

THE PENNSYLVANIA STATE UNIVERSITY  
SCHREYER HONORS COLLEGE

DEPARTMENT OF BIOMEDICAL ENGINEERING

DEVELOPMENT OF A MICRO-PARTICLE IMAGE VELOCIMETRY PLATFORM TO  
STUDY THROMBOSIS IN VITRO

TICE R. HARKINS  
SPRING 2019

A thesis  
submitted in partial fulfillment  
of the requirements  
for a baccalaureate degree  
in Premedicine  
with honors in Biomedical Engineering

Reviewed and approved\* by the following:

Keefe Manning  
Associate Dean for Academic Affairs, Schreyer Honors College  
Professor of Biomedical Engineering and Surgery  
Thesis Supervisor

William Hancock  
Chair of the Intercollege Graduate Program in Bioengineering  
Professor of Biomedical Engineering  
Honors Adviser

Ronald Markle  
Director, Premedicine and General Science Majors  
Professor of Biology  
Thesis Reader

\* Signatures are on file in the Schreyer Honors College.

## ABSTRACT

Cardiovascular disease is the number one cause of death in the United States, affecting over 600,000 people annually. Many cardiovascular diseases are thought to be caused by a microcirculatory dysfunction. Micro-scale alterations to the blood flow pathway through an implant (e.g. left ventricular assist device, artificial stents, and valves) are one of the known factors that contribute to clot formation. Understanding these micro-scale factors that cause thrombosis is of paramount importance.

Few studies have examined flow patterns around geometric irregularities and their effect on coagulation. The goal of this study was to quantify the flow pathway and set up a platform to visualize thrombus development in two channels constructed from a transparent plastic, PDMS. Each channel had a geometric irregularity, crevice or sudden expansion, which served as a nidus of thrombus formation. To quantitatively measure flow, a micro-particle image velocimetry ( $\mu$ PIV) system was coupled with an inverted epi-fluorescent microscope. Due to the nature of  $\mu$ PIV, whole blood could not be used as the fluid medium. A solution to this problem was the use of reconstituted blood composed of tracer-particle seeded plasma and ghost erythrocyte cells in which the hemoglobin and cellular components were removed to achieve optical transparency.

The data demonstrated the technique's ability to generate stable flows within each PDMS channel. Flow maps obtained support the  $\mu$ PIV system's ability to quantitatively measure flow within a PDMS channel. A backward facing step was observed to greatly reduce the flow speed immediately after the site of expansion. A small crevice was also shown to produce regions of flow stagnation that could increase platelet residency time and promote the adherence of platelets.

## TABLE OF CONTENTS

LIST OF FIGURES .....	iii
LIST OF TABLES .....	iv
ACKNOWLEDGEMENTS .....	v
Chapter 1 Introduction .....	1
1.1 Clinical Need.....	1
1.2 Platelet Activation and Function .....	4
1.3 Thrombosis.....	6
1.4 Surface Irregularities .....	9
1.5 Objective .....	11
Chapter 2 Design of Micro-Particle Image Velocimetry System .....	12
2.1 Micro-Particle Image Velocimetry Theory .....	12
2.2 Microscope Assembly .....	13
Chapter 3 Methods .....	15
3.1 PDMS Channel Manufacturing.....	15
3.2 Blood Analog Preparation.....	20
3.3 Fluid Perfusion .....	22
3.4 Image Acquisitions and Analysis.....	25
3.5 Experimental Design.....	32
Chapter 4 Results .....	35
4.1 Technique Validation Experiment .....	35
4.2 Blood Analog Experiment.....	39
Chapter 5 Discussion .....	45
5.1 Validation of Technique.....	45
5.2 Blood Analog .....	47
5.3 Limitations and Future Research .....	49
BIBLIOGRAPHY .....	51
ACADEMIC VITA.....	57

## LIST OF FIGURES

Figure 1-1: The development of a thrombus within the HeartMate II VAD. (A) only fibrin. (B) fibrin and blood clot. (C) side-view of blood clot (D) blood clot <sup>9</sup> .....	2
Figure 1-2: CarboMedics mitral valve prosthetic. A large thrombus (right) completely immobilizes the flap (seen without obstruction, left) <sup>25</sup> .....	3
Figure 1-3: Scanning electron microscopy images of a resting platelet (left) and an activated platelet (right) <sup>31,32</sup> .....	5
Figure 1-4: The titanium alloy material of an LVAD can adsorb proteins like albumin, fibronectin, and fibrinogen <sup>26</sup> .....	5
Figure 1-5: The coagulation cascade. Platelet derived tissue factor facilitates the activation of factor X, which then converts prothrombin to thrombin <sup>13</sup> .....	7
Figure 1-6: A cardiovascular device induces the formation of a thrombus when it comes into contact with blood <sup>28</sup> .....	8
Figure 1-7: Computed streamlines and wall shear rate at a main channel shear rate of $400 \text{ s}^{-1}$ <sup>17</sup> .....	10
Figure 2-1: PIV system. Fluid moving through a channel is seeded with tracer particles. The displacement of particles is recorded over a known time step so that the velocity may be obtained for every integration region <sup>34</sup> .....	13
Figure 2-2: A schematic image of a $\mu$ PIV system setup <sup>34</sup> .....	14
Figure 3-1: Overview of the master mold and PDMS channel manufacturing protocol <sup>39</sup> .....	17
Figure 3-2: Plasma cleaning changes the surface chemistry of the PDMS and glass cover slide to facilitate their adhesion <sup>40</sup> .....	17
Figure 3-3: Dimensions of the backward facing step model as viewed from the top. The brown face is the top of the structure. The direction of flow is bottom to top. ....	18
Figure 3-4: Dimensions of the crevice model as viewed from the top. The brown face is the top of the structure. The direction of flow is bottom to top.....	19
Figure 3-5: Whole blood separated into components. PRP and PPP are represented as plasma <sup>19</sup> ..	20
Figure 3-6: Blood analog containing ghost RBCs at 20% hematocrit as seen through our microscope using bright field illumination at 20X magnification. Direction of flow is bottom to top. ....	22
Figure 3-7: (A) Observed vs. Expected Flow Rate. (B) Validation of $1 \text{ }\mu\text{L/min}$ flow rate. (C) Validation of $20 \text{ }\mu\text{L/min}$ flow rate. Observed flow Rate was recorded as mass of fluid displaced after 5 minutes at the expected flow rate. ....	24

Figure 3-8: Blood analog being perfused through a crevice PDMS channel.....	25
Figure 3-9: Each grid is one interrogation window. An integration window is 64 x 64 pixels. The highlighted region in the center is within the processing mask. ....	28
Figure 3-10: Vector Field generated in a backward facing step model at 1 $\mu\text{L}/\text{min}$ . Green vectors are valid. Yellow vectors are interpolated from a smoothing function.....	29
Figure 3-11: Vector Fields generated from (A) 10 images, (B) 50 images (C) 200 images without smoothing function and (D) 200 images with smoothing function. Green = valid vector, red = bad vector, yellow = interpolated vector.....	30
Figure 3-12: Vector Fields generated from (A) 10 images, (B) 50 images (C) 200 images without smoothing function and (D) 200 images with smoothing function. Green = valid vector, red = bad vector, yellow = interpolated vector.....	31
Figure 3-13: Percentage of vectors labeled valid as a function of the number of image pairs processed. (A) Data obtained in a crevice channel at 1 $\mu\text{L}/\text{min}$ flow rate. (B) Backward facing step at the same experimental conditions.....	32
Figure 3-14: Velocity profiles were acquired from points along three lines. (A) Line at Y = -0.3 mm and is upstream of the crevice. (B) Line at Y = 0.-15 mm and is within the crevice (C) Line at Y = -0.05 mm and is downstream of the crevice. ....	33
Figure 4-1: Flow within the crevice channel at 1 $\mu\text{L}/\text{min}$ . Velocity profiles were obtained from the positions labeled A, B, and C.....	36
Figure 4-2: Velocity magnitude vs. X – Position in the crevice channel.....	37
Figure 4-3: Flow within the backward facing step channel at 1 $\mu\text{L}/\text{min}$ . Velocity profiles were obtained from the positions labeled A, B, and C. ....	38
Figure 4-4: Velocity magnitude vs. X – Position in the backward facing step channel. ....	39
Figure 4-5: Flow within the crevice channel at 20 $\mu\text{L}/\text{min}$ . The fluid used was platelet-rich plasma. Velocity profiles were obtained from the positions labeled A, B, and C.....	40
Figure 4-6: Flow within the crevice channel at 20 $\mu\text{L}/\text{min}$ . The fluid used was 20% ghost cell hematocrit bovine blood. Velocity profiles were obtained from the position labeled A, B, and C.....	41
Figure 4-7: Velocity magnitude vs. X – Position in the crevice channel at 20 $\mu\text{L}/\text{min}$ flow rate. The velocity profiles of PRP and 20% Hct bovine blood were compared.....	43
Figure 4-8: A comparison of the percentage of valid vectors by fluid used. For each measurement, 200 image pairs were averaged without the use of a smoothing function. ....	44
Figure 5-1: Computational simulation of fluid flowing adjacent to a crevice at $\text{Re} = 100$ . A region of stagnant to near stagnant flow can be observed within the crevice <sup>42</sup> .....	46

Figure 5-2: Computational simulation of a velocity profile in a backward facing step model.  $Re = 242$ . There is a region of slow flow after the expansion<sup>43</sup> .....47

Figure 5-3: Regions of burnt pixels skewed data collection. A smoothing function was able to mask these regions, however the actual flow vectors in the regions highlighted in red on the left were not calculated. ....50

## LIST OF TABLES

Table 3-1: Summary of the velocity validation experiment.....	33
Table 3-2: Summary of the blood analog experiment.....	34

## ACKNOWLEDGEMENTS

I would first like to thank my thesis supervisor, personal mentor, and dear friend, Dr. Keefe Manning. The support and guidance that he provided made writing this thesis possible. I would also like to thank the many other members of the Artificial Heart Lab. Thank you to Kristen Hagenah for formally introducing me to independent research. Thank you also to Jeremy Myslowski and Josh Kessler for spending countless hours with me in 110 Hallowell trying to assemble this system. I would also like to thank Dr. Bryan Good and Sailahari Ponnaluri for answering my many questions and always offering to help. I also thank Connor Watson for helping collect data and manufacture PDMS channels. I would like to extend a heartfelt thank you to Josh Riley and Nicole Price for providing support. In the Penn State Nanofabrication lab I would like to thank Guy Lavallee for training me on lab protocols and helping me to manufacture needed equipment for this study. In Hallowell I would like to thank Gene and Gary for providing lots of assistance. I would also like to thank the Penn State Erickson Discovery Grant and the Schreyer Honors College for providing financial support for this project. Finally, I would like to thank all members of my family for their unwavering support through the tough process that is college. Thank you to my mother Ellie, my father Kevin, my brother Harry, and my sister Megan.



## **Chapter 1**

### **Introduction**

#### **1.1 Clinical Need**

Cardiovascular disease (CVD) is the number one cause of death in the United States, affecting over 600,000 people annually<sup>1</sup>. Patients suffering from end-stage CVD often require the implantation of an artificial device to maintain adequate blood circulation and oxygen delivery to tissues<sup>2</sup>. Congestive heart failure, in which the heart no longer pumps enough blood to supply the body, is best treated with heart transplantation. However, there currently exists a greater demand for heart transplants than there is a source of matching donors<sup>3</sup>. Therefore, there is a clinical need to support patients suffering from congestive heart failure until a donor can be found. Left ventricular assist devices (LVADs) serve as a life-saving device and a bridge to transplant for patients without a donor. While LVADs are effective in pumping blood to the systemic circuit, which is crucial to supply tissues with oxygen, these devices are marked with increased thrombogenicity<sup>3</sup>. The device can induce the formation of life-threatening blood clots in the patient<sup>4</sup>. Blood clots within the HeartMate II VAD can be seen in Figure 1-1.

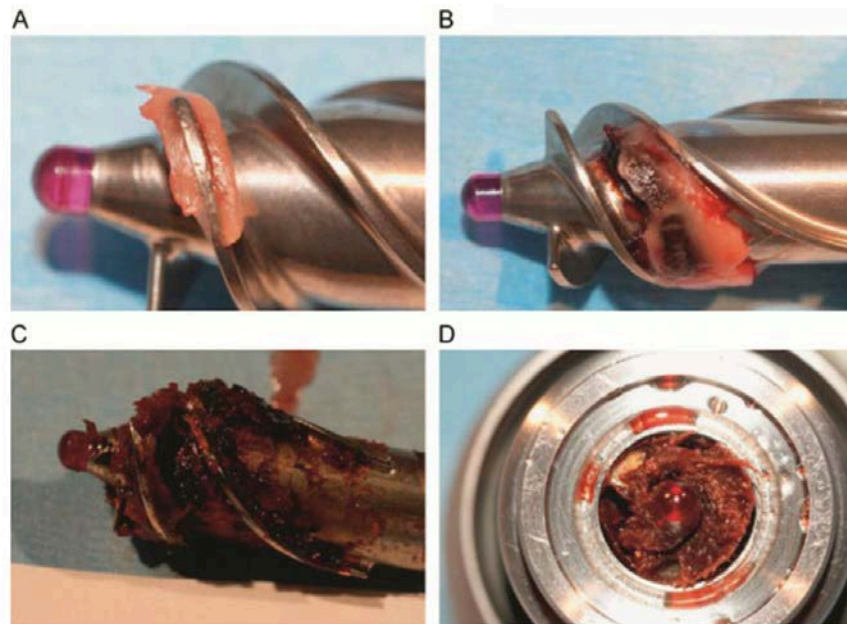


**Figure 1-1:** The development of a thrombus within the HeartMate II VAD. (A) only fibrin. (B) fibrin and blood clot. (C) side-view of blood clot (D) blood clot<sup>9</sup>.

Other common CVDs include aortic and mitral valve disease. Heart valve disease affects around 5 million Americans per year<sup>5</sup>. When the heart valve becomes compromised due to disease, the valve can no longer function properly as the maintainer of unidirectional flow between heart chambers. As a result, regurgitation is observed. A treatment of this disease involves the implantation of a prosthetic valve to replace the native diseased tissue. This process is usually successful in combating unwanted backward blood flow, however there is a 0.3 to 1.3 % chance per patient-year that the prosthetic heart valve will cause life-threatening thrombosis<sup>6</sup>. Prosthetic valve thrombosis (PVT) is depicted in Figure 1-2.

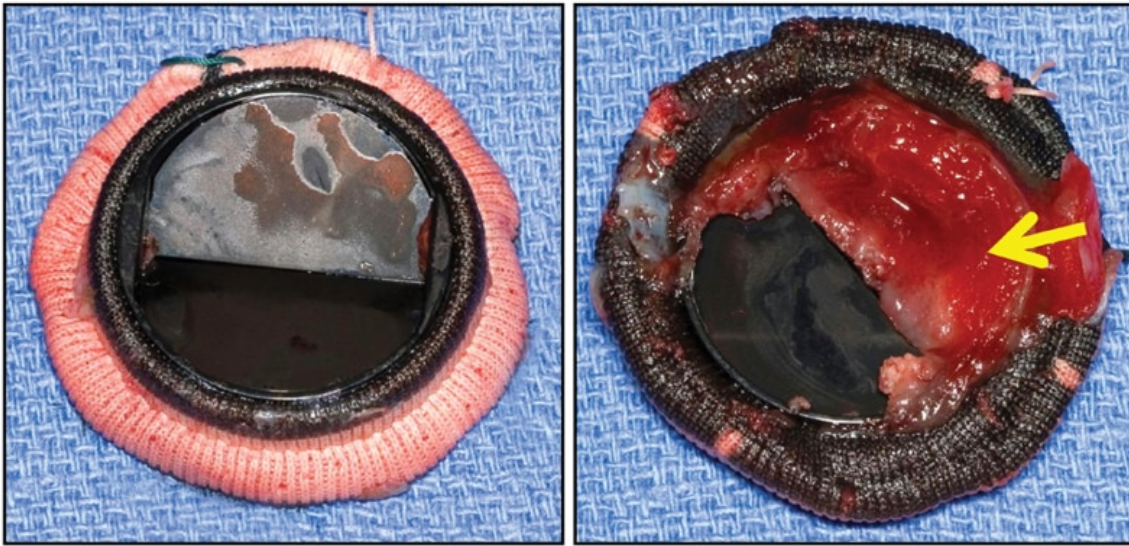


**Figure 1-2:** CarboMedics mitral valve prosthetic. A large thrombus (right) completely immobilizes the flap (seen without obstruction, left) <sup>25</sup>.

Another common CVD is the accumulation of plaque in the coronary artery, the artery that supplies blood to the heart. To treat the narrowing of this artery, expandable stents are used to widen the vessel causing an increase in blood flow. Artificial stents can also promote coagulation, although this is a somewhat rare occurrence. Only 1.3% of patients experience stent thrombosis, but when this happens 45% of those cases are fatal<sup>7</sup>.

Although VADs, valves, and stents maintain life in the short term, these devices can induce the formation of life threatening blood clots<sup>3,4,5,6,7,8</sup>. There is currently intense study in the field of cardiovascular devices aimed at reducing the thrombogenic potential of implants to improve the quality of life for the patients in which the devices are deployed. Furthermore, enhancing the hemocompatibility of these devices would extend their supportive capabilities as a bridge to transplantation.

## 1.2 Platelet Activation and Function

Platelets are anucleated circulating formed elements, typically 1-2 microns in diameter. A scanning electron micrograph of a normal and activated platelet can be seen in Figure 1-3. A normal platelet count is on the order of  $5 \times 10^{10}$  platelets per liter of blood plasma<sup>9</sup>. The function of a platelet is to act as the first responder in the process of hemostasis. When the endothelial layer of a vessel is damaged, platelets adhere to exposed basement membrane proteins, specifically collagen and fibulin-1<sup>26</sup>. Once a platelet becomes deposited, it changes shape and begins to secrete chemical markers like adenosine diphosphate (ADP), thromboxane A<sub>2</sub>, and tissue factor, which all promote more platelet activation and deposition. This process forms the platelet plug, which is essential to preserve a pressurized circulatory system.

Platelet activation is an extremely important factor when considering the hemocompatibility of a device. Patients that have an implanted LVAD have been documented to possess supraphysiological numbers of activated platelets<sup>27</sup>. The primary mechanism for platelet activation within an LVAD is shear stress at the blood-material interface. Platelets that are activated by this shear stress then adhere to deposited proteins like von Willbrand Factor and fibrinogen as shown in Figure 1-4.

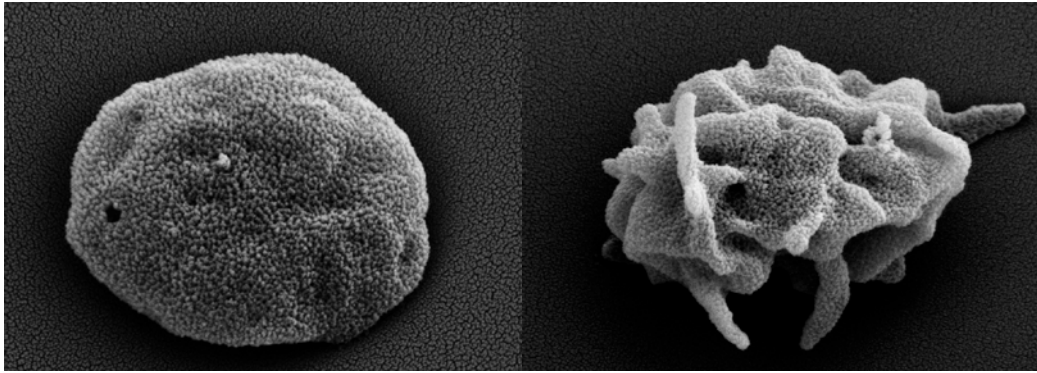


**Figure 1-3:** Scanning electron microscopy images of a resting platelet (left) and an activated platelet (right) <sup>31,32</sup>.

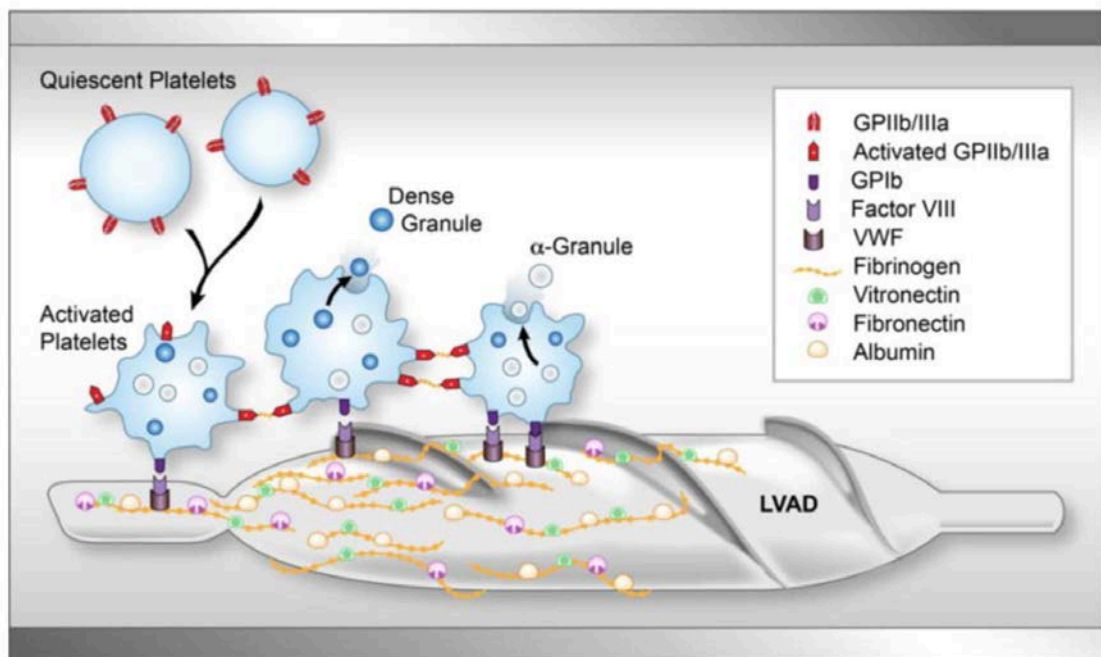


**Figure 1-4:** The titanium alloy material of an LVAD can adsorb proteins like albumin, fibronectin, and fibrinogen<sup>26</sup>.

### 1.3 Thrombosis

One of the responses of a platelet to adherence is secretion of micro-particles into the surrounding blood plasma. These micro-particles contain tissue factor (TF)<sup>29</sup>. Tissue factor then forms an activated complex with factor VIIa, which then leads to activation of factor X. This process can be understood as the tissue activation pathway in the coagulation cascade shown in Figure 1-5. The activation of factor X then promotes the conversion of prothrombin to thrombin. Activated thrombin cycles back in a positive feedback loop to activate more platelets and also catalyzes the reaction converting plasma soluble fibrinogen to the insoluble fibrin. Fibrin strands create a dense mesh that can trap erythrocyte cells passing through the blood and also help to stabilize the network of platelets.

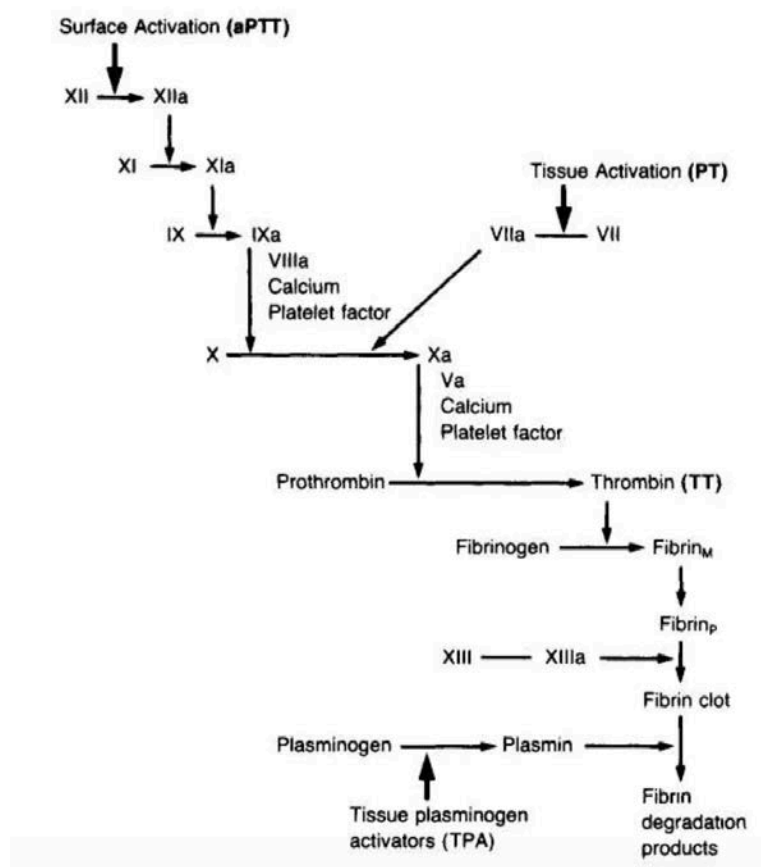


**Figure 1-5:** The coagulation cascade. Platelet derived tissue factor facilitates the activation of factor X, which then converts prothrombin to thrombin<sup>13</sup>.

Activation of the coagulation cascade can be caused by tissue factor release like the process described previously or by surface activation. When a foreign material like a VAD, valve, or stent is introduced into the blood stream, plasma soluble proteins will adhere to the surface and promote further coagulation. This process can be seen in Figure 1-6. The life threatening thrombosis usually associated with artificial device use is due, in part, to this adverse reaction of the blood to the foreign material. Patients who have an implanted device are usually prescribed anticoagulants or antiplatelet medication<sup>35</sup>. Two commonly prescribed anticoagulants are heparin and warfarin. Heparin activates antithrombin, ultimately making thrombin inactive. If



thrombin is inactive, then fibrinogen will stay in its plasma soluble form. Warfarin acts to block vitamin K. Usually vitamin K activates prothrombin and factor VII, however in the presence of warfarin it does not. Long-term use of heparin has been related to low platelet counts and therefore, it is not used as a long-term treatment. Even with these treatments, some patients still develop life-threatening thrombosis.

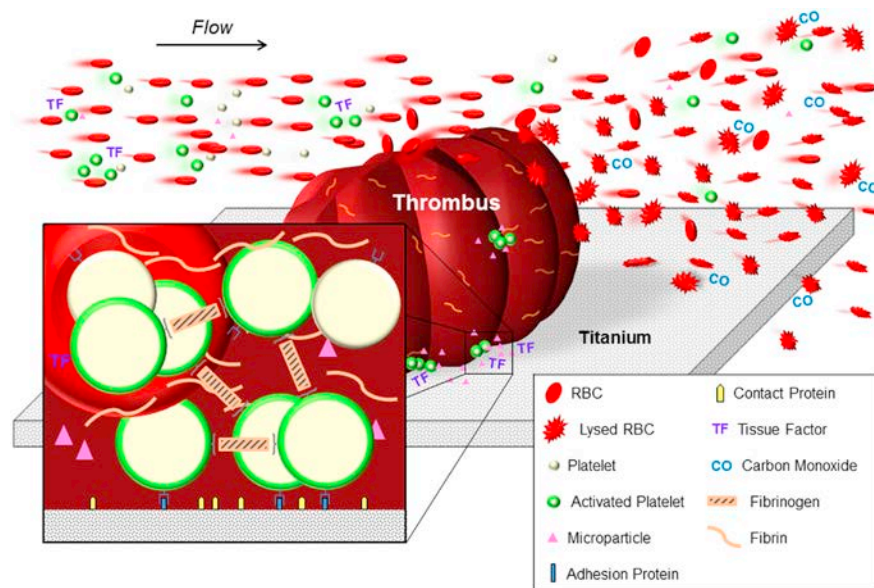


**Figure 1-6:** A cardiovascular device induces the formation of a thrombus when it comes into contact with blood<sup>28</sup>.

Recent studies have leveraged the controlled and reproducible environment provided by microfluidic channels to study thrombosis. A study conducted at the Colorado School of Mines fabricated a polydimethylsiloxane (PDMS) channel in order to determine the way in which a blood clot forms to seal a blood vessel from the external environment in the case of injury to the



vessel. Results from their study indicated that a PDMS chamber and fluorescent imaging technique could be used to study the deposition of platelets and fibrin in real time<sup>36</sup>.

#### **1.4 Surface Irregularities**

The blood flow pathway through a blood-contacting medical device is critical when considering the hemocompatibility of the device. Irregularities on the surface of a material, even microscopic ones, can promote platelet activation and adherence<sup>13</sup>. Recent studies have investigated platelet deposition to crevices of a defined size. A small manufacturing error or imperfect machining can cause small crevices on the surface of an otherwise macroscopically smooth material. These crevices can be found on the titanium alloy (Ti6Al4V) material, of which many cardiovascular devices are constructed. An irregularity will invariably cause altered blood flow. Previous studies done by Jamiolkowski *et al.* have computed the expected flow pathways within a crevice and quantified actual platelet deposition onto a crevice in real time. Figure 1-7 shows the computed streamlines within a crevice with dimensions of 90 microns across by 122 microns in depth.

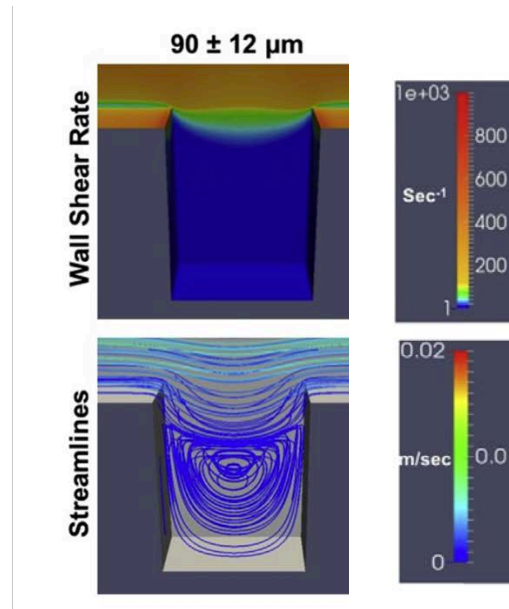


**Figure 1-7:** Computed streamlines and wall shear rate at a main channel shear rate of  $400 \text{ s}^{-1}$  <sup>17</sup>.

A small crevice was found to promote platelet adhesion. The region of highest platelet accumulation was in the downstream corner of the crevice near the main channel. The shear rate was also an important factor for platelet adhesion to a crevice. Lower shear, around  $400 \text{ s}^{-1}$ , was observed to promote increased platelet adherence compared to a higher shear rate of  $1000 \text{ s}^{-1}$ . Other studies have aimed to determine the effect of micro-scale topological changes and their effects on the hemocompatibility of arterial heart valves. One such study fabricated a PDMS channel designed to imitate the finger-like topology of fine cilia. The PDMS had small protrusions approximately 150 nm in diameter. The results of the study found that surface topology does indeed contribute to platelet activation. Textured surfaces significantly reduced the number of adsorbed proteins and adherent platelets by reducing the amount of surface area available for the platelet to contact<sup>30</sup>. In a study conducted by Siedlecki's group at the Pennsylvania State University College of Medicine, sub-micron texturing with ordered arrays of

pillars was used to reduce platelet adhesion to polyether urethane urea by manufacturing sub-platelet sized features on the surface<sup>33</sup>.

## **1.5 Objective**

The goal of this study was to quantify the flow pathway in two PDMS channels using bovine platelet-rich plasma and reconstituted bovine blood at 20% ghost cell hematocrit. Each channel had a geometric feature, a crevice or backward facing step, which served as a nidus of irregular flow patterns. The crevice feature can be commonly found in the titanium alloy of a VAD<sup>17</sup>. A backward facing step feature was designed after a computational coagulation study at the macro-scale<sup>45</sup>. The effect of fluid composition on flow behavior was observed. Information gained from this study was used to better understand the interaction of blood with geometric irregularities at the micro-scale and in order to ultimately create more biocompatible cardiovascular devices.

## Chapter 2

### Design of Micro-Particle Image Velocimetry System

#### 2.1 Micro-Particle Image Velocimetry Theory

Micro-particle image velocimetry (PIV) allows for fluid flow to be visualized and quantified. This technique uses an Nd:YAG 532 nm laser (New Wave Research, Inc., Fremont, CA) set to emit two discrete light pulses at a known time interval known as  $\Delta T$ . To collect PIV data, the fluid of interest must be seeded with passive tracer particles (Thermo Fischer Scientific, Waltham, MA). Tracer particles are polystyrene beads embedded with fluorescent dye. The fluorescent dye excites at 540 nm, and emits a longer wavelength of light at 560 nm. The diameter of a tracer particle is one micron. The movement of these particles is assumed to be representative of the fluid in which they are suspended. Light from a laser pulse is diffused through the microscope objective and illuminates the entire volume of fluid above the microscope's objective. Particles that travel through this illumination emit light of a longer wavelength that can be separated from the laser light by the addition of long pass mirrors. A Laserpulse synchronizer (TSI, Shoreview, MN) couples the firing of a laser with the capturing of an image by a Powerview 4MP-HS CCD camera (TSI, Shoreview, MN). When the light pulse is emitted, the camera takes the first image, frame A, then at precisely  $\Delta T$  seconds later, the second light pulse is emitted and another image is taken, frame B. These frames are then stored on a Dell Precision T7400 (Dell, Round Rock, TX) to be processed later. A depiction of a PIV system is shown in Figure 2-1.

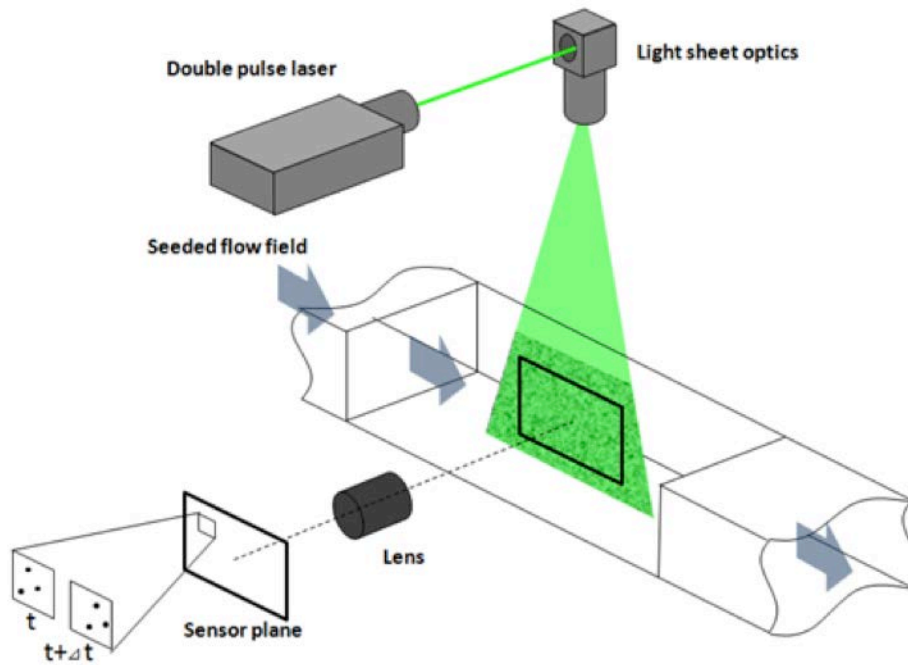


**Figure 2-1:** PIV system. Fluid moving through a channel is seeded with tracer particles. The displacement of particles is recorded over a known time step so that the velocity may be obtained for every integration region<sup>34</sup>.

## 2.2 Microscope Assembly

Micro-particle image velocimetry ( $\mu$ PIV) requires the addition of an inverted epifluorescent microscope alongside the laser, synchronizer, and camera system described previously. A Nikon Eclipse TE300 microscope (Nikon, Melville, NY) with a Plan Fluor 20X (Nikon, Melville, NY) objective is attached to the laser via a liquid light guide (TSI, Shoreview, MN). In between the fluid of interest and the camera is a filter cube that separates the laser light from the light emitted by the particles. In this study, a Nikon eclipse filter cube equipped with the ET-532nm laser bandpass set was used. In  $\mu$ PIV there is no two-dimensional light sheet as shown in Figure 2-1. Instead, the entire volume of fluid passes through the laser light. A

consequence of this is that particles are illuminated above and below the microscope's focal plane. A representative image is shown in Figure 2-2.

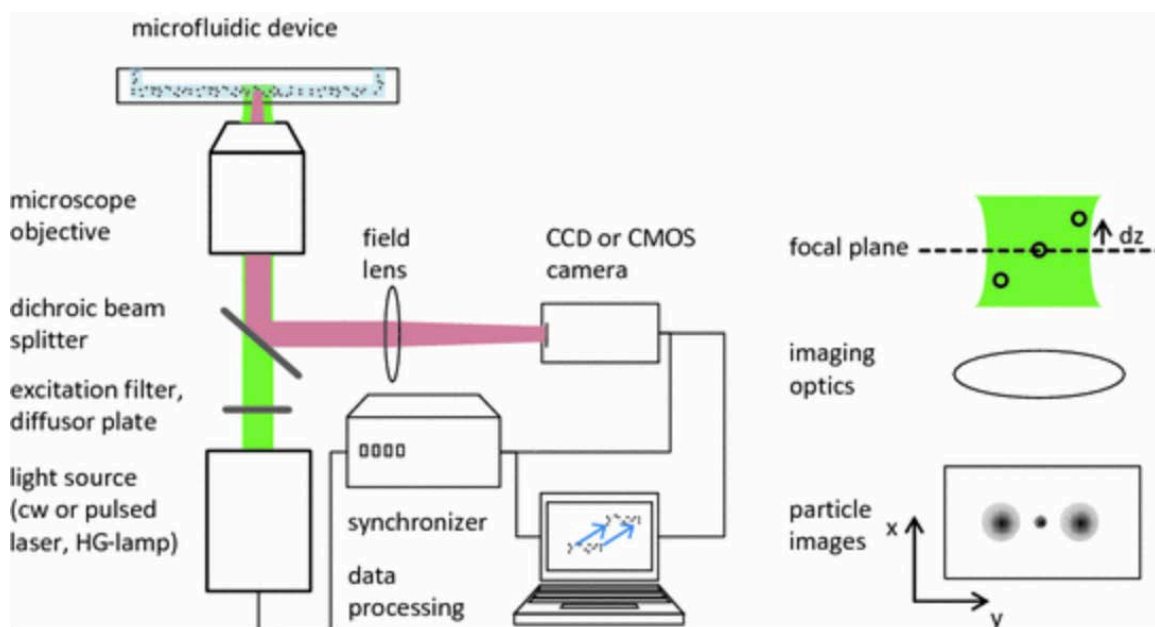


**Figure 2-2:** A schematic image of a  $\mu$ PIV system setup<sup>34</sup>.

## **Chapter 3**

### **Methods**

#### **3.1 PDMS Channel Manufacturing**

Two customized polydimethylsiloxane (PDMS) channels were designed for this study. These channels each contained one feature. One channel contained a backward facing step. One channel contained a crevice. Dimensions for these two channels were first entered electronically into Solid Works ® (SolidWorks Corp., Waltham, MA) and then transferred to the Penn State Nanofabrication Laboratory for the creation of a master mold by photolithography. To manufacture a master mold, the base is coated with SU-8 photoresist (Thermo Fischer Scientific, Waltham, MA) in a process known as spin coating. Spin coating consists of two main steps. In the first step, the aluminum base is coated with a layer of SU-8. Next, the base is spun at 1000 rpm for 30 seconds. Spinning the base ensures an even coating of SU-8. Then the base and photoresist are placed under a mask and exposed to UV light. The mask ensures that only the desired sections of the photoresist are exposed to UV light. SU-8 photoresist forms cross links in the presence of UV light and becomes hard. UV exposed SU-8 will stick to the base while non-exposed sections that were under the mask will wash off during the post expose bake. The photolithographic procedure for PDMS device manufacture can be seen in Figure 3-1.

After the master-mold had been completed, PDMS channels could be created by first mixing 50 mL of SYLGARD® silicone elastomer base with 10 mL of silicone elastomer curing agent (Dow Chemical Company, Midland, MI). The PDMS mixture was then stirred for 10

minutes and poured onto the master mold. The mold and PDMS were then placed inside of a vacuum chamber for 30 minutes in order to de-gas the silicone mixture. After de-gassing, the mold was moved onto a hot plate (Thermo Fischer Scientific, Waltham, MA) for 20 minutes at 150 °C to allow the plastic to cure. Next, the PDMS was removed from the mold and a 1 mm hole was punched into the inlet and outlet ports of the chamber using a 1mm hole punch (Miltex, York, PA). Finally, the channel was completed by placing a glass microscope slide (VWR, Radnor, PA) and the PDMS in a plasma cleaner (Harrick Plasma Inc, Ithaca, NY) for 5 minutes. Plasma cleaning the PDMS converts the  $-\text{OSi}(\text{CH}_3)_2$  units into silanol groups ( $-\text{OH}$ )<sup>40</sup>. Once the oxidized PDMS comes into contact with  $-\text{OH}$  groups on the glass slide, a dehydration reaction binds the two surfaces creating an airtight seal, as shown in Figure 3-2. The main flow channel is 400 x 10 microns (width x height) and 50 mm in length. The channel includes one feature at the halfway point of the channel's length. In the backward facing step (BFS) model, the main channel size is reduced to 200 x 10 microns at the location of the step. The BFS model is displayed in Figure 3-3. The other channel has a crevice of dimension 90 x 122 microns added to the side of the wall, as shown in Figure 3-4.



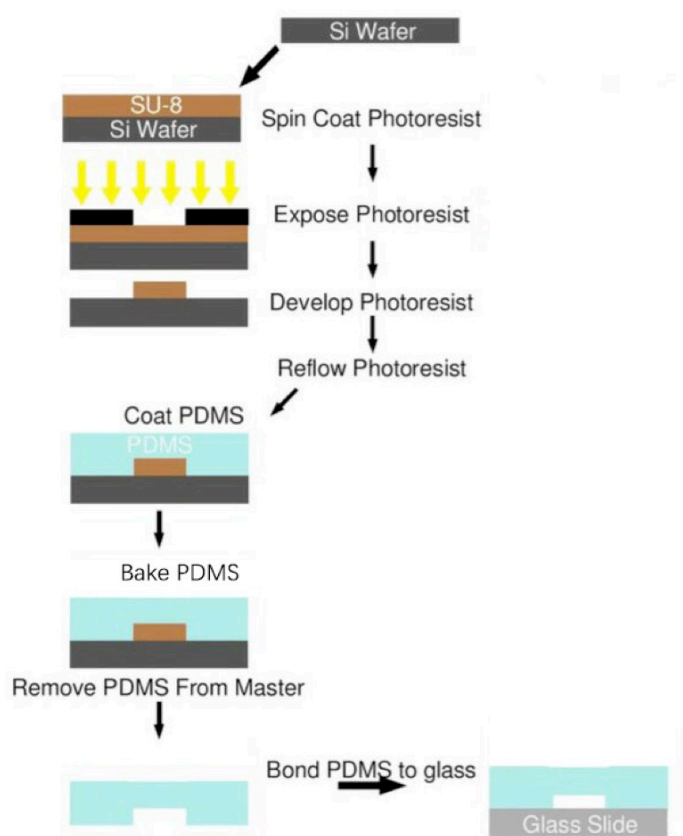


**Figure 3-1:** Overview of the master mold and PDMS channel manufacturing protocol<sup>39</sup>.

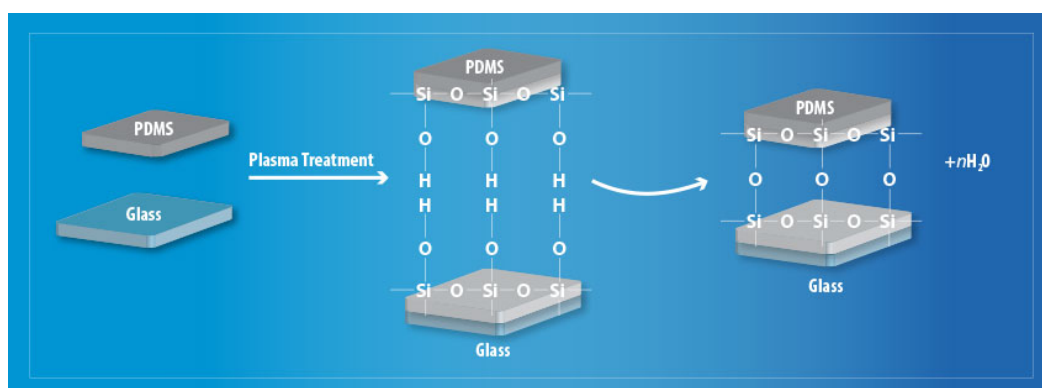


**Figure 3-2:** Plasma cleaning changes the surface chemistry of the PDMS and glass cover slide to facilitate their adhesion<sup>40</sup>.

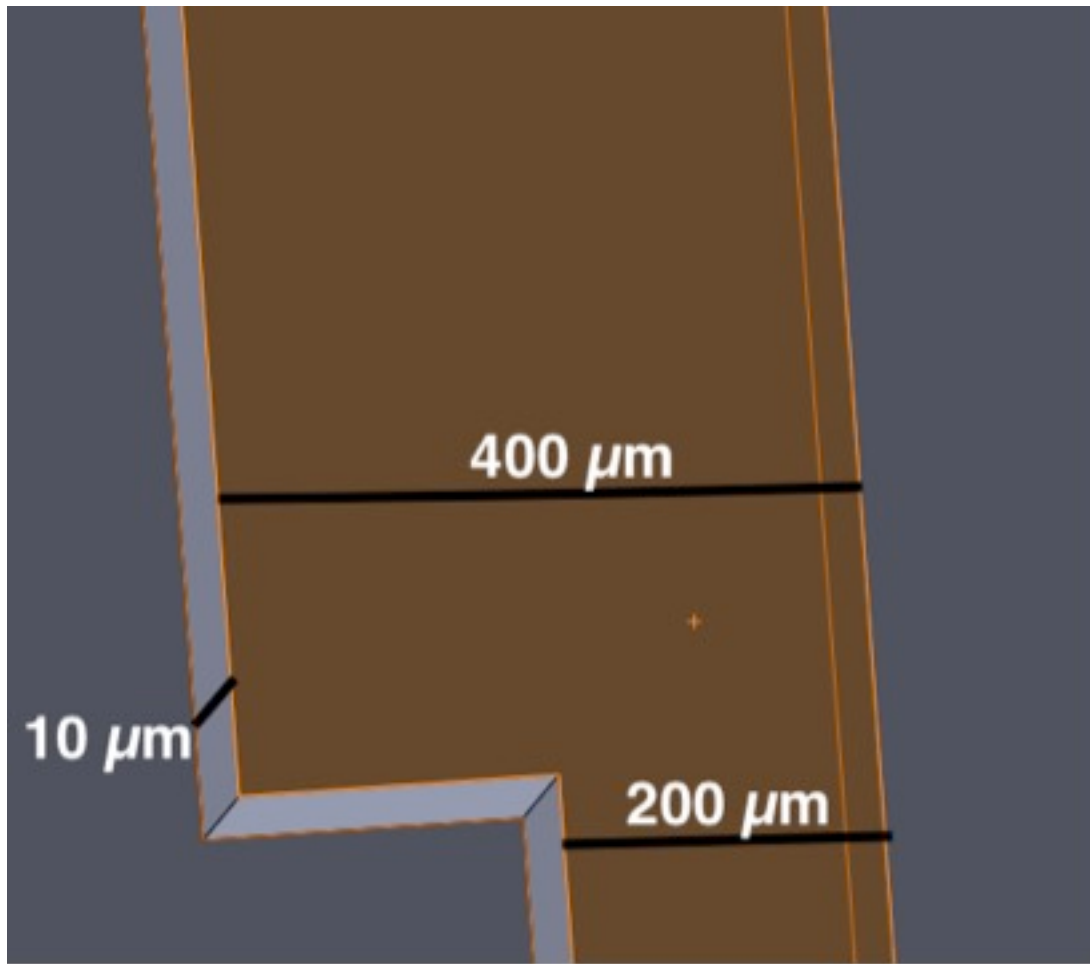


**Figure 3-3:** Dimensions of the backward facing step model as viewed from the top. The brown face is the top of the structure. The direction of flow is bottom to top.

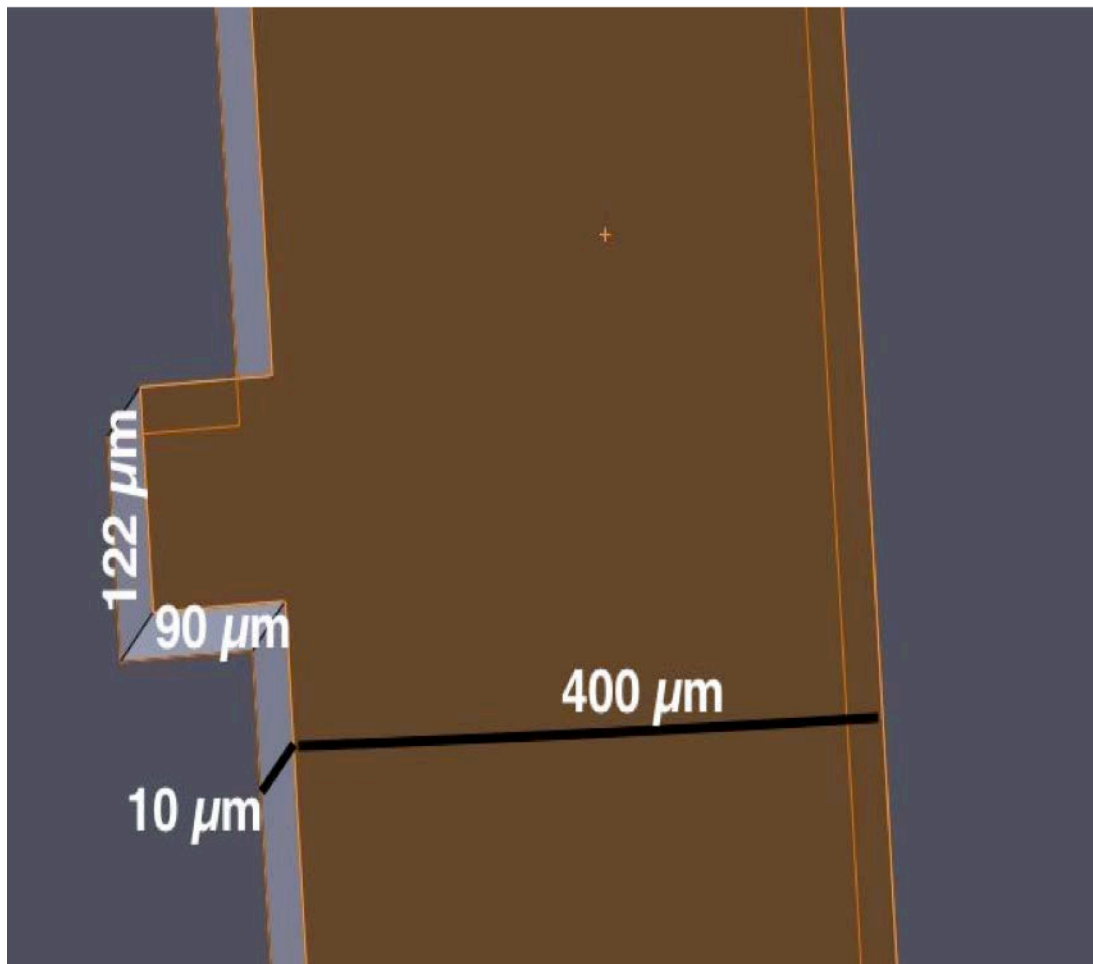


**Figure 3-4:** Dimensions of the crevice model as viewed from the top. The brown face is the top of the structure. The direction of flow is bottom to top.

### 3.2 Blood Analog Preparation

Whole blood was collected from a bovine donor in accordance with IACUC protocols for humane and safe use. In this study two tubes were used to contain bovine blood. For larger blood samples a 50 mL Falcon tube was used (Becton Dickinson, Franklin Lakes, NJ). For smaller samples a 12 mL tube (VWR Radnor, PA) was used. Platelet-rich plasma (PRP) was collected by centrifugation of 50 mL of whole bovine blood at 600 g for 12 minutes. Platelet-poor plasma (PPP) was then isolated by further centrifugation at 1500 g for 20 minutes. For all centrifugation cycles, an Eppendorf 5810R centrifuge (Eppendorf, Hauppauge, NY) was used. After the PPP was removed, a buffy white coat could be found on top of the bovine red blood cells (RBCs). The white coat was discarded leaving behind bovine RBCs. The average proportions of these components in whole blood are depicted in Figure 3-5.

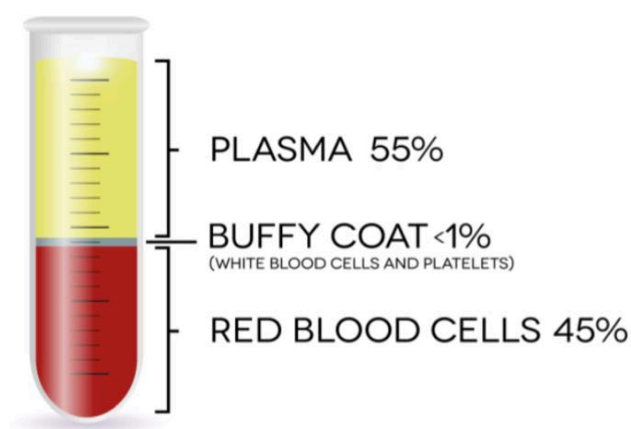


**Figure 3-5:** Whole blood separated into components. PRP and PPP are represented as plasma<sup>19</sup>.

Once RBCs were isolated and then purified using successive washing with phosphate buffered saline (PBS) (Thermo Fischer, Waltham, MA) bovine erythrocyte ghosts could be

synthesized in accordance with a previously established protocol<sup>20</sup>. The protocol requires 10 mL of purified RBCs diluted in 10 mL of 1 X PBS (Thermo Fischer, Waltham, MA). The 50:50 cell:saline solution was then incubated in a hypotonic lysing solution. The lysing solution was composed of magnesium sulfate (VWR, Radnor, PA) at a concentration of 0.5 g/L and 5 X PBS at 30 mL/L at a pH of 5.2 achieved by titrations with glacial acetic acid (Thermo Fischer, Waltham, MA). The purpose of this solution was to lyse the cell membrane and draw out hemoglobin and other cellular components. Five minutes later, the cell containing lysing solution was brought back to physiological osmolality by addition of Tris HCl [1M] pH 8.5 (GBiosciences, St. Luis, MO) and 5 x PBS. The solution is then cooled to 0 °C and stored overnight. The following morning the solution is incubated in a 37 °C water bath (Thermo Fischer Scientific, Waltham, MA) for one hour to allow the ghost RBC membranes to reseal. After the cell membranes reseal, the ghost cells are separated from the lysing solution by centrifugation. When hemoglobin is removed from an RBC, the resulting ghost cell maintains the rheological properties of a native RBC while at the same time being optically transparent<sup>13</sup>. Ghost RBCs within a micro scale channel can be seen in Figure 3-6.

The final step in blood analog preparation was to recombine the separated blood components and add passive tracer particles. Mixing 2 mL of ghost RBCs with 8 mL of PRP made a 20% hematocrit blood analog. Adding 10 uL of tracer particle containing solution to this analog allowed for the fluid flow to be quantified in our system.

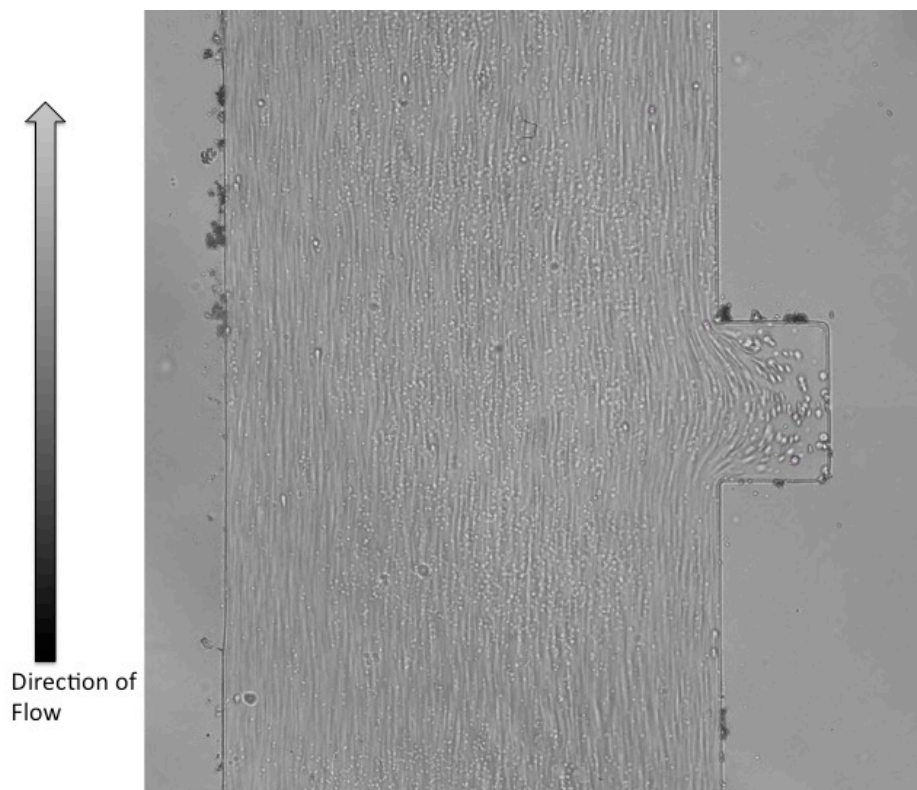


**Figure 3-6:** Blood analog containing ghost RBCs at 20% hematocrit as seen through our microscope using bright field illumination at 20X magnification. Direction of flow is bottom to top.

### 3.3 Fluid Perfusion

In this study, deionized water, PRP, and 20% ghost cell erythrocyte bovine blood were used as the fluid for experiments. The fluid was drawn into a 3mL syringe (Becton Dickinson, Franklin Lakes, NJ). This syringe was then placed into a KD Scientific syringe pump (KD Scientific Inc., Holliston, MA) capable of pushing fluid through the system at a known and adjustable flow rate. The flow rates used were 1  $\mu\text{L}/\text{min}$  and 20  $\mu\text{L}/\text{min}$ . An experiment was conducted to calibrate the syringe pump. Figure 3-7 displays the results of this study. An input flow rate of 1  $\mu\text{L}/\text{min}$  mapped to an average observed flow rate of  $0.90 \pm 0.0548$  (SEM)  $\mu\text{L}/\text{min}$ . An input flow rate of 20  $\mu\text{L}/\text{min}$  resulted in an average observed flow rate of  $19.72 \pm 0.2417$

(SEM)  $\mu\text{L}/\text{min}$ . Once the syringe was secured in the pump, a Tygon tube (VWR, Radnor, PA) was connected on one end to the syringe and at the other to the PDMS channel. Blood flow through a Tygon tube to the PDMS channel can be seen in Figure 3-8.

Reynolds number was calculated using Equation 1. In this equation,  $\rho$  is the fluid density,  $V$  is the velocity of the fluid (as determined from the flow rate)  $D_H$  is the hydraulic diameter and  $\mu$  is the dynamic viscosity of the fluid. The hydraulic diameter is equivalent to four times the flow area divided by the perimeter of the flow chamber. The Reynolds number in a capillary ranges from 0.001 to 0.09<sup>41</sup>. The Reynolds number within the PDMS device used in this study was 0.19 at a flow rate of 1  $\mu\text{L}/\text{min}$ . The experimental Reynolds number was more than twice the Reynolds number found in a capillary or small arteriole.

$$Re = \frac{\rho V D_H}{\mu} \quad (1)$$

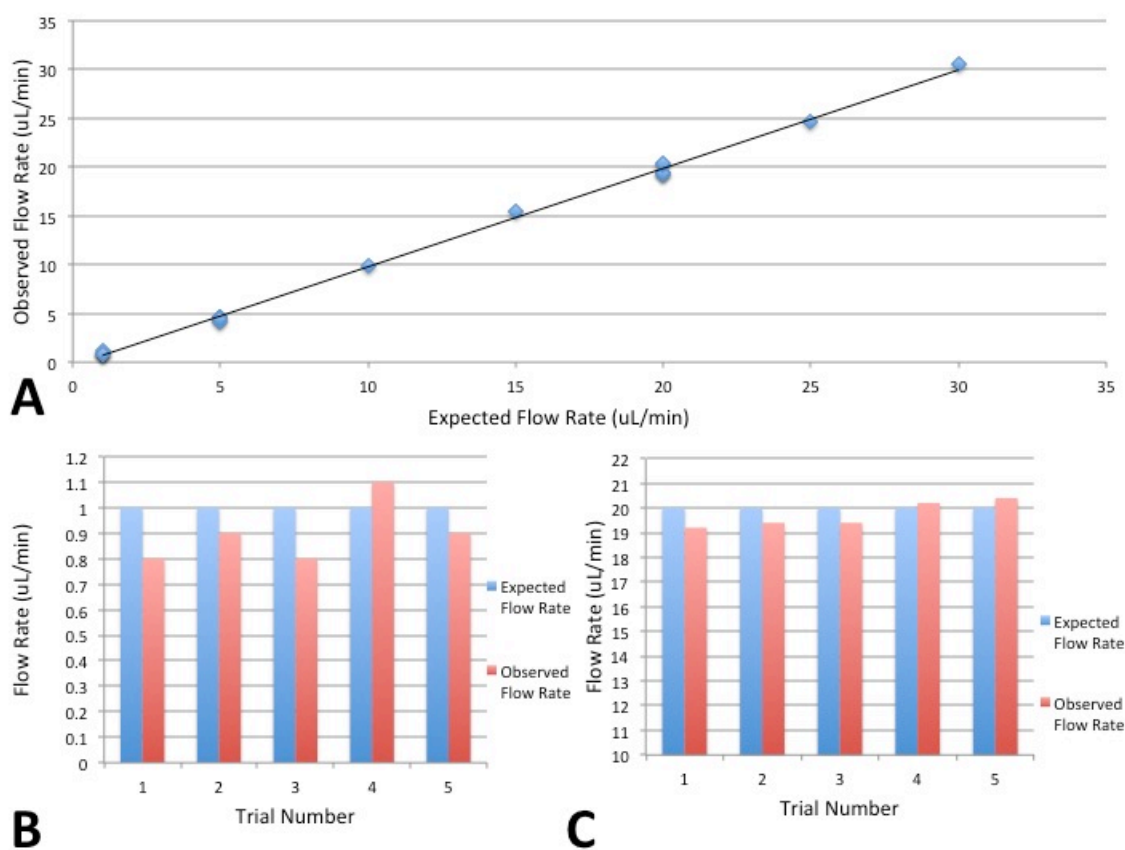


**Figure 3-7:** (A) Observed vs. Expected Flow Rate. (B) Validation of 1  $\mu\text{L}/\text{min}$  flow rate. (C) Validation of 20  $\mu\text{L}/\text{min}$  flow rate. Observed flow Rate was recorded as mass of fluid displaced after 5 minutes at the expected flow rate.



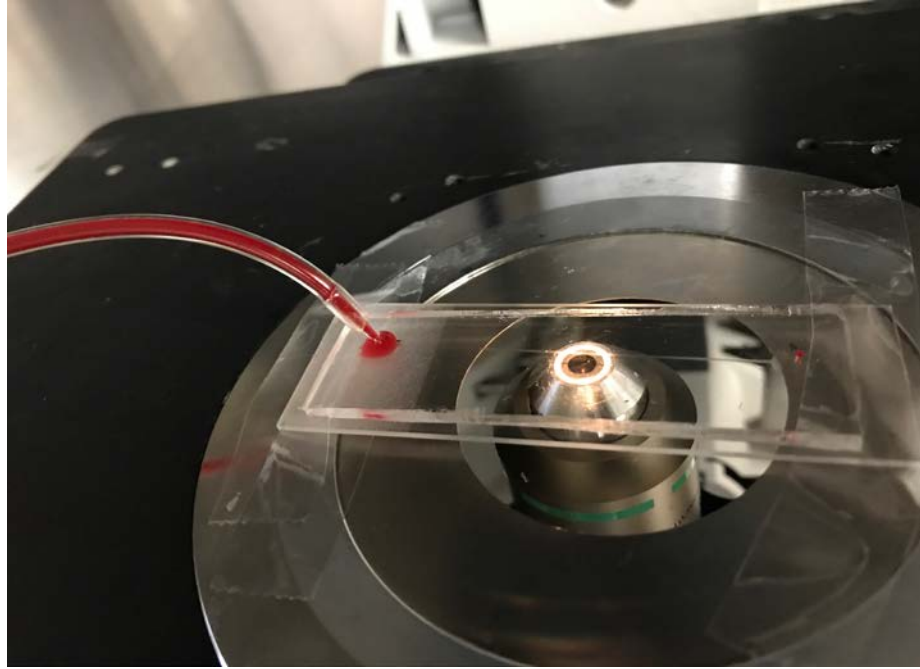


**Figure 3-8:** Blood analog being perfused through a crevice PDMS channel.

### 3.4 Image Acquisitions and Analysis

In this study, Insight 4G (TSI, Shoreview, MN) was used as the image acquisition and processing software. The first step for the acquisition of an image pair is to set the timing diagram. The  $\Delta T$  must be set such that the particles move about a quarter to a third of an interrogation window, shown in Figure 3-9. Different  $\Delta T$  values were used in each experiment. When the flow rate is increased, the  $\Delta T$  must be decreased in order to keep average particle displacement constant. Equation 2 describes the relationship between the flow rate and  $\Delta T$ .  $Q$  is the volumetric flow rate ( $\text{m}^3/\text{s}$ ),  $A$  is the cross-sectional area of the PDMS device ( $\text{m}^2$ ), and  $x$  is the length of one side of the square interrogation window. This equation ensures that the particles have moved  $1/3$  of an interrogation window on average. If the  $\Delta T$  is too high, the particles will

move out of one window and the software will be unable to track their velocity. If the  $\Delta T$  is too low, the particles will not move enough and their velocity will not be recorded accurately. Once the timing diagram is set, image acquisition can begin. For each experiment 200 image pairs are taken at a rate of 14.5 Hz.

$$\frac{Q}{A} \Delta T = \frac{1}{3} x \quad (2)$$

When image acquisition was complete, the analysis procedure could begin. First, the spatial dimensions of the image were calibrated. This was accomplished by measuring a known distance on the image. For this study the PDMS chamber was used as the reference since it was known to be exactly 400  $\mu\text{m}$  wide. The spatial calibration of the field of view was 0.46 mm wide by 0.35 mm long. Next, all 200 images pairs were preprocessed. Preprocessing images removed background noise by creating a black and white image. In the preprocessed image, the background was black and the particles were white. Next the processing mask was applied to each image pair. The mask ensures that the computer processes only the region of interest of each photo. An example mask is shown in Figure 3-9. Finally, the data were processed. In the processing procedure, the displacement of each particle was calculated by measuring the distance traveled between frame A and B. Since the time in-between frames was exactly  $\Delta T$  seconds, the velocity of each particle could be calculated. If there are multiple particles in an interrogation window, the average displacement was calculated and used to generate a representative vector. A two-dimensional vector field generated by this method can be observed in Figure 3-10. For ensemble PIV processing, vectors calculated within each image pair were averaged and the

degree to which INSIGHT was confident in its generated vector field increases as more image pairs were averaged. The relationship between image pairs processed and the percent of vectors determined to be valid by the software is shown in Figure 3-11, Figure 3-12 and Figure 3-13. As more image pairs were processed, the resulting vector field had a higher percentage of valid vectors. In the last step, a smoothing function was applied to correct the remaining 1-2% of bad vectors. The smoothing function consisted of three steps. The first step consisted of a global vector validation. Vectors that were outside of three standard deviations from the global mean were discarded. The second step consisted of a local vector validation. The local mean in a 30 x 30 micron area was calculated. Within each local cluster, vectors that fell more than three standard deviations from the local mean were discarded. Finally a local vector-conditioning phase interpolated vectors from valid vectors to replace bad vectors.

Once a vector field had been made, the data could be post-processed in Tecplot® (Tecplot Inc, Bellevue, WA). In Tecplot the data could be visually represented to show both the magnitude and direction of each vector. In Tecplot the background color represents the magnitude of the velocity. The direction that the fluid traveled was shown by the addition of arrows. These arrows were not the computer-generated vectors. Arrows in Tecplot served as a visual aid and could be manipulated to show general trends in the velocity profile. Tecplot was also used to extract lines from a two-dimensional graph in order to create graphs of velocity magnitude vs. X position at a fixed Y position.

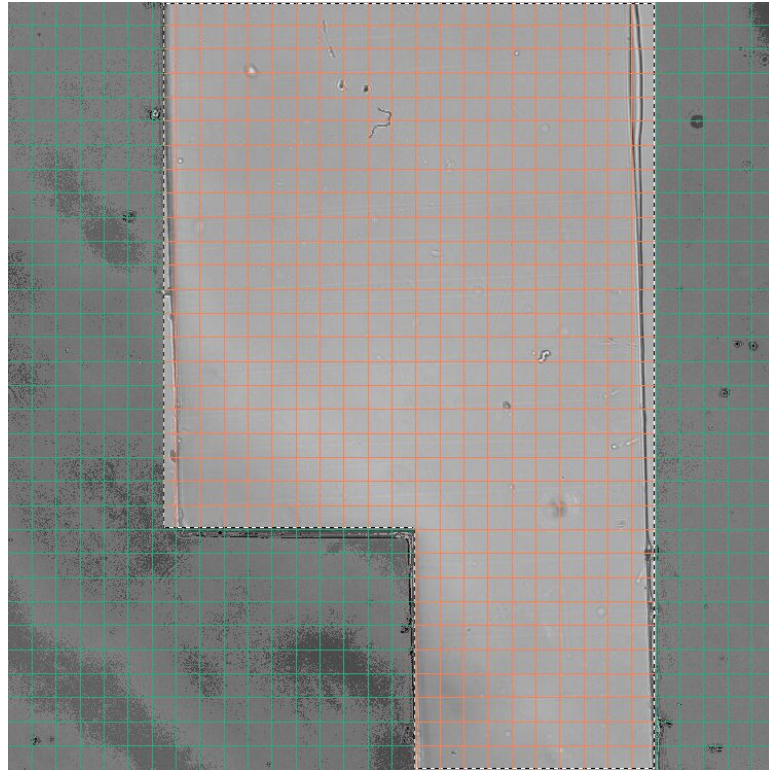


**Figure 3-9:** Each grid is one interrogation window. An integration window is 64 x 64 pixels. The highlighted region in the center is within the processing mask.

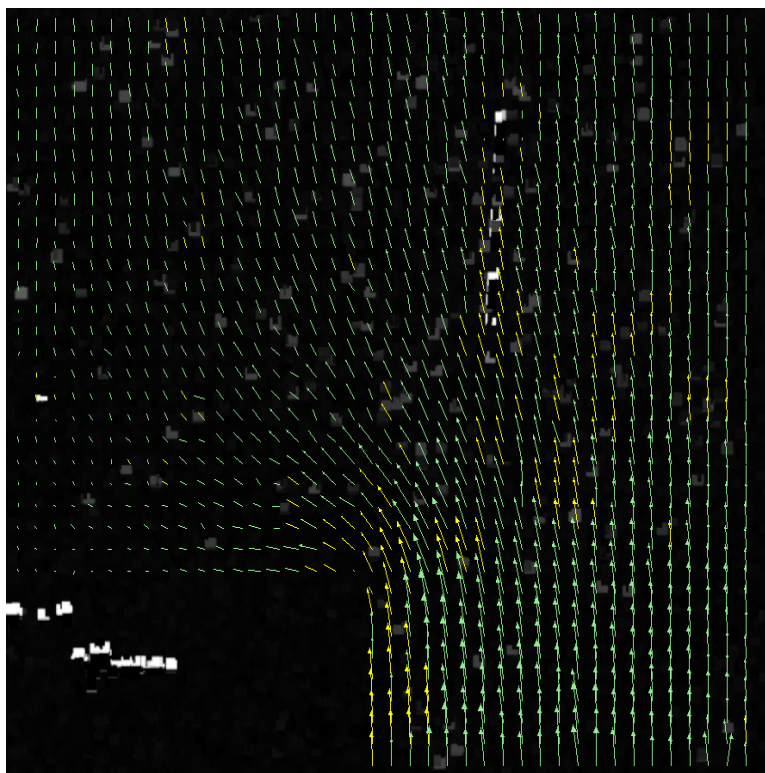


**Figure 3-10:** Vector Field generated in a backward facing step model at 1  $\mu\text{L}/\text{min}$ . Green vectors are valid. Yellow vectors are interpolated from a smoothing function.

## Crevice

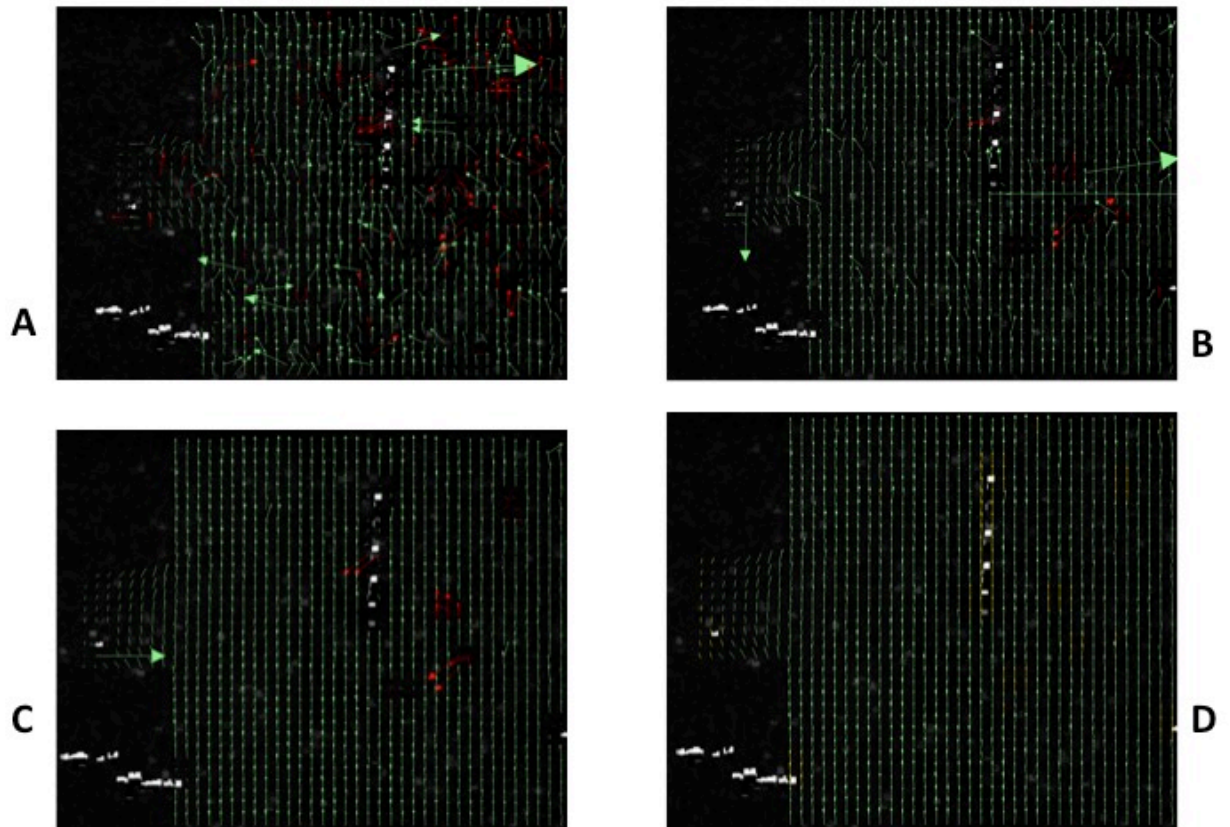


**Figure 3-11:** Vector Fields generated from (A) 10 images, (B) 50 images (C) 200 images without smoothing function and (D) 200 images with smoothing function. Green = valid vector, red = bad vector, yellow = interpolated vector.



### Backward facing step

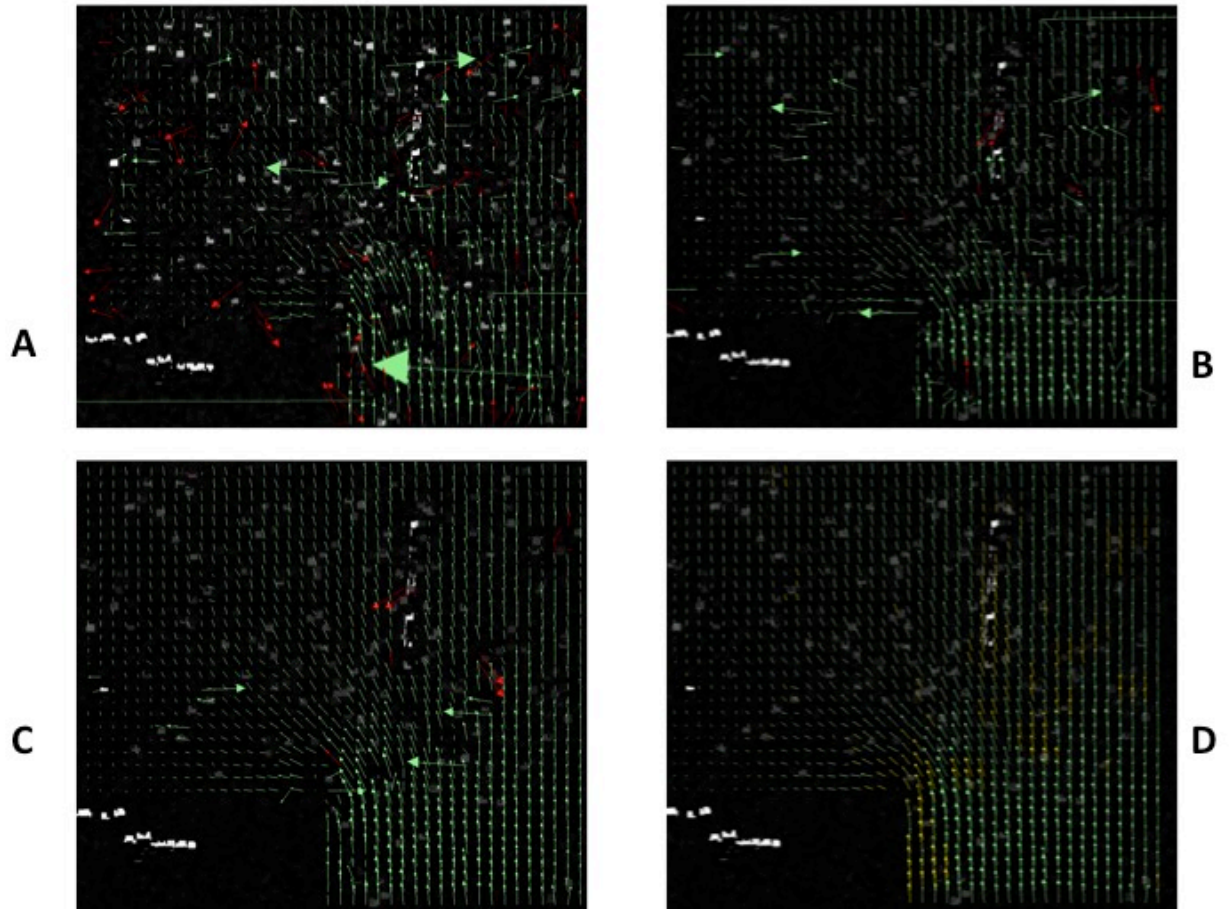


**Figure 3-12:** Vector Fields generated from (A) 10 images, (B) 50 images (C) 200 images without smoothing function and (D) 200 images with smoothing function. Green = valid vector, red = bad vector, yellow = interpolated vector.

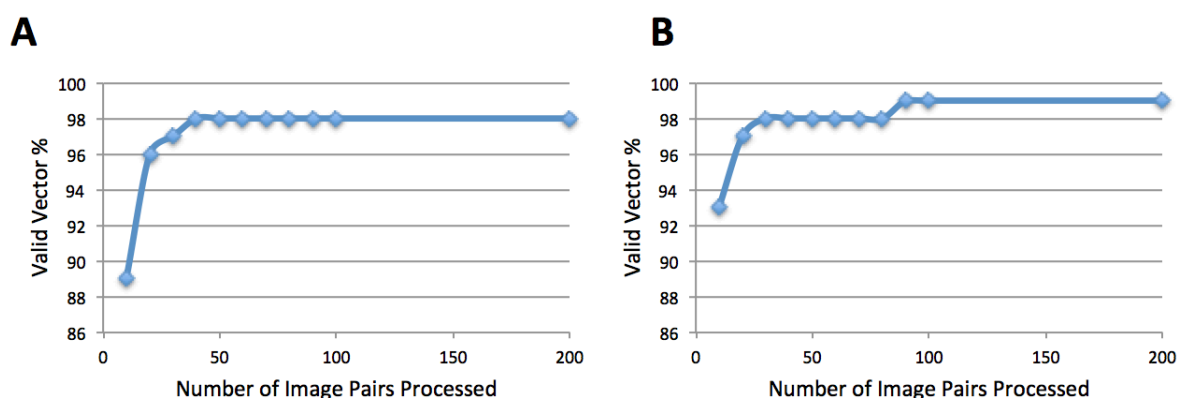


**Figure 3-13:** Percentage of vectors labeled valid as a function of the number of image pairs processed. (A) Data obtained in a crevice channel at 1  $\mu\text{L}/\text{min}$  flow rate. (B) Backward facing step at the same experimental conditions.

### 3.5 Experimental Design

Testing was divided into two phases. In the first phase, the goal was to validate the  $\mu\text{PIV}$  technique's ability to generate an accurate two-dimensional vector field. A relatively slow flow rate of 1  $\mu\text{L}/\text{min}$  was used in order to minimize the pressure at the inlet. Low pressure at the inlet reduced the risk of fluid injection failure. When fluid injection fails the flow through the channel is not constant. If the flow is not constant then the data obtained will have a large percentage of bad vectors. To validate the technique, one, two-dimensional vector field was generated within each channel. From this two-dimensional vector field, velocity profiles were obtained at fixed Y positions as shown in Figure 3-14. A line was acquired at  $Y = -0.3 \text{ mm}$ ,  $Y = -0.15 \text{ mm}$ , and  $Y = -0.05 \text{ mm}$ . The line extracted was used to create a plot of velocity magnitude vs. X position. Velocity magnitude plots were then used to compare flow profiles before, within, and after the geometric irregularity present within each channel.



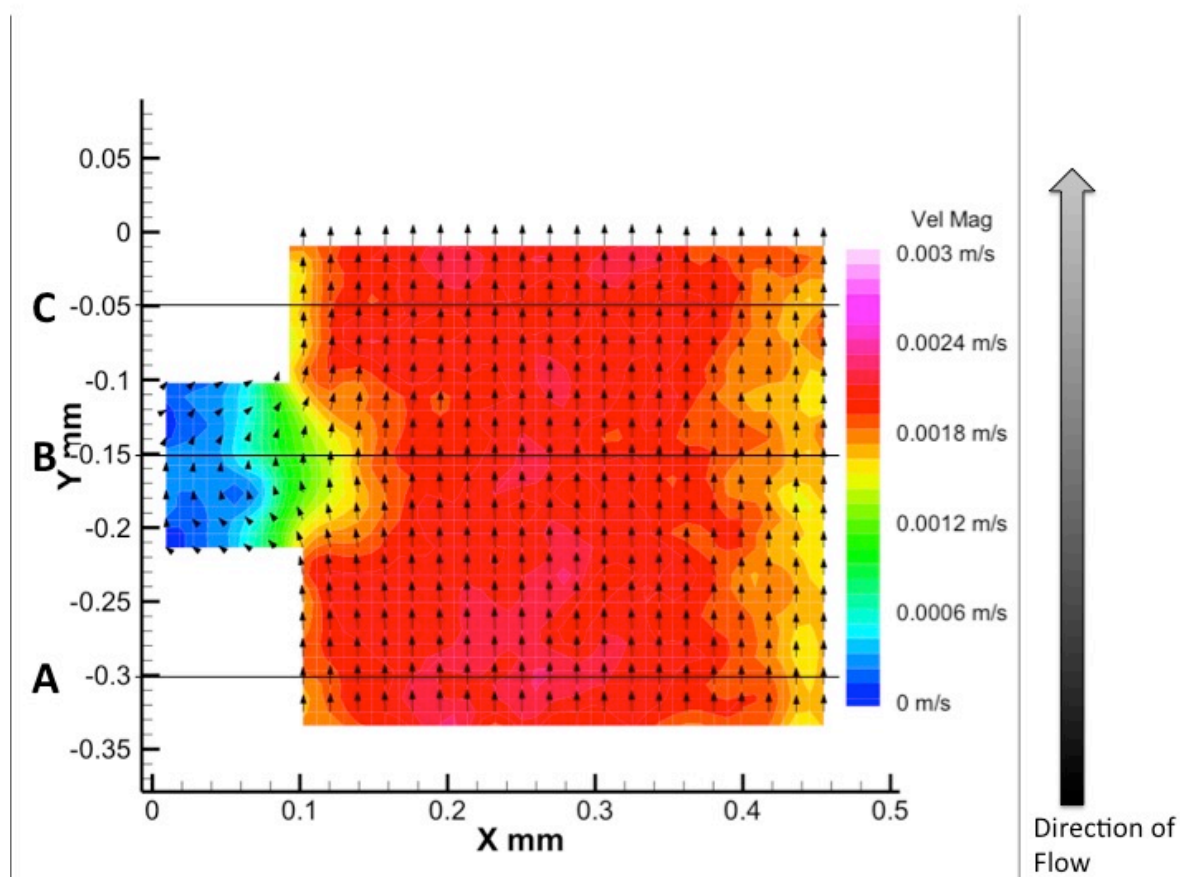


**Figure 3-14:** Velocity profiles were acquired from points along three lines. (A) Line at  $Y = -0.3$  mm and is upstream of the crevice. (B) Line at  $Y = -0.15$  mm and is within the crevice (C) Line at  $Y = -0.05$  mm and is downstream of the crevice.

**Table 3-1:** Summary of the velocity validation experiment

Channel Type	Fluid Used	Fluid Viscosity <sup>37</sup> (cP)	Flow Rate ( $\mu\text{L}/\text{min}$ )	Concentration of Tracer Particles	$\Delta T$	Reynolds number
Crevice	diH <sub>2</sub> O	0.7195	1	1%	1600	0.195
Backward Facing Step	diH <sub>2</sub> O	0.7195	1	1%	1200	0.190

After validating the system using diH<sub>2</sub>O, the next experimental phase sought to determine if  $\mu\text{PIV}$  measurements could be made using a more viscous and less transparent fluid. In phase

two of testing, the PDMS channel used and flow rate were kept constant and the fluid was changed. The two fluids tested were PRP and 20% ghost cell hematocrit blood. The crevice model channel was used because previous studies have tested platelet adhesion in crevices of the same size. Velocity profiles from lines at a fixed Y value were obtained using the same process explained and depicted previously. The percentage of valid vectors in each vector field will be analyzed in order to determine if using a more viscous and opaque fluid affects the quality of data.

**Table 3-2:** Summary of the blood analog experiment

Channel Type	Fluid Used	Fluid Viscosity <sup>38</sup> (cP)	Flow Rate (μL/min)	Concentration of Tracer Particles (v/v)	ΔT (μs)	Reynolds Number
Crevice	PRP	1.2	20	1%	75	2.08
Crevice	20% ghost cell Hct bovine blood	2.5	20	1%	75	2.15

## Chapter 4

### Results

#### 4.1 Technique Validation Experiment

The fluid used for this experiment was diH<sub>2</sub>O. Velocity profiles were plotted to determine the flow regime. Figure 4-1 displays a Tecplot graph of the vector field generated within the crevice model at 1  $\mu$ L/min. The lines, labeled A, B, and C, correspond to velocity profiles A, B, and C, respectively in Figure 4-2. In the crevice model, data from the line at Y = -0.30 mm (location A) shows that the fluid is stable and laminar before entering the crevice region of the channel. The mean velocity of fluid before the crevice is 1.99 mm/s. The velocity profile is altered by the crevice. At Y = -0.15 mm (location B), the velocity magnitude of the fluid is observed to be much slower within the crevice compared to the main channel. The mean velocity at location B is 1.60 mm/s. Data show that the slowest flow region is furthest from the main channel at X = 0.02 mm. As the distance from the back wall of the crevice increases, the velocity of fluid also increases. Downstream of the crevice, at Y = -0.05 mm (location C) the mean velocity magnitude of the fluid increases to 1.93 mm/s. The velocity profile before and after the crevice are nearly identical in mean velocity. For the velocity profiles at locations A and C, X = 0.10 mm corresponds to the wall. In location B at X = 0.10 mm the crevice-channel boundary is found. At X = 0.10 mm, locations A and C depict a velocity magnitude of 1.77 mm/s and 1.70 mm/s respectively. At location B within the crevice the velocity magnitude is reduced to 1.21

mm/s at  $X = 0.10$ . At location B along the back wall of the crevice furthest away from the main channel ( $X = 0.018$ ) the velocity magnitude is 0.25 mm/s.

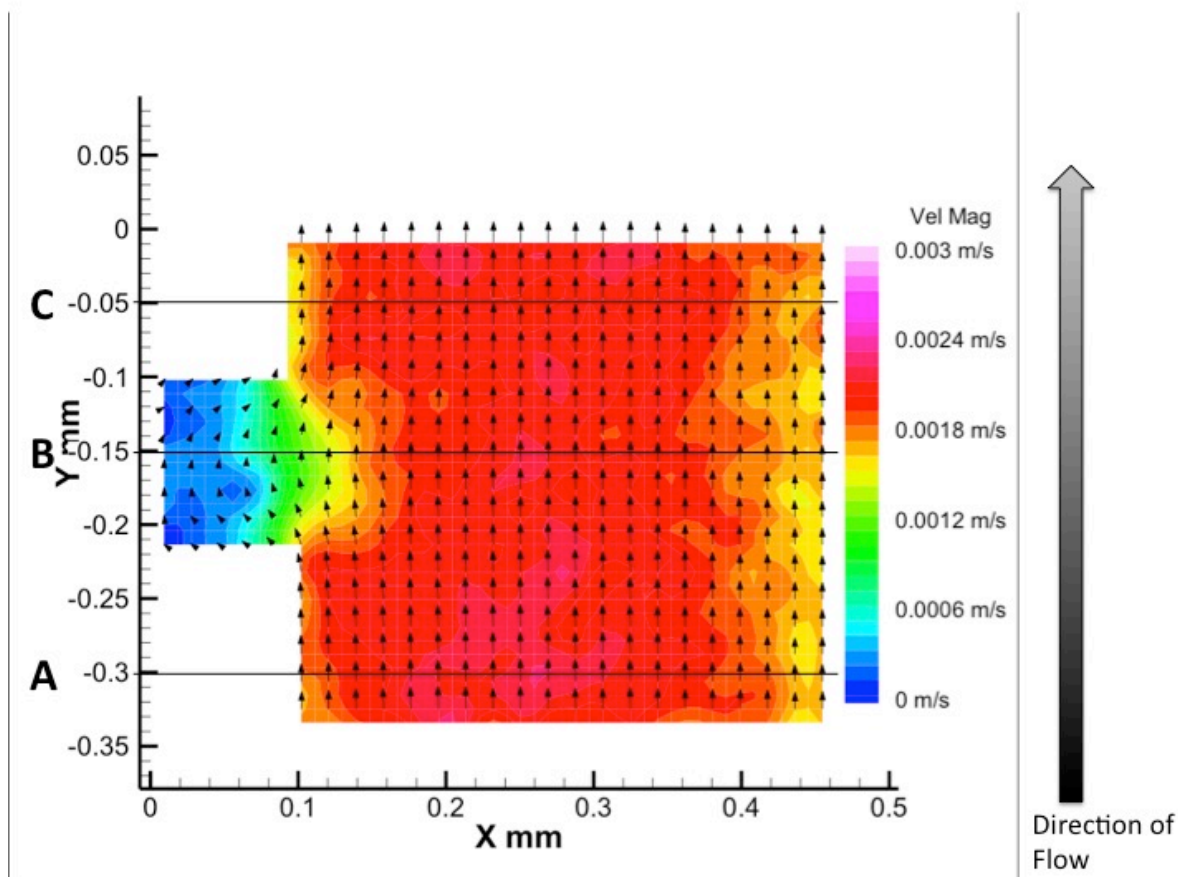


**Figure 4-1:** Flow within the crevice channel at 1  $\mu\text{L}/\text{min}$ . Velocity profiles were obtained from the positions labeled A, B, and C.

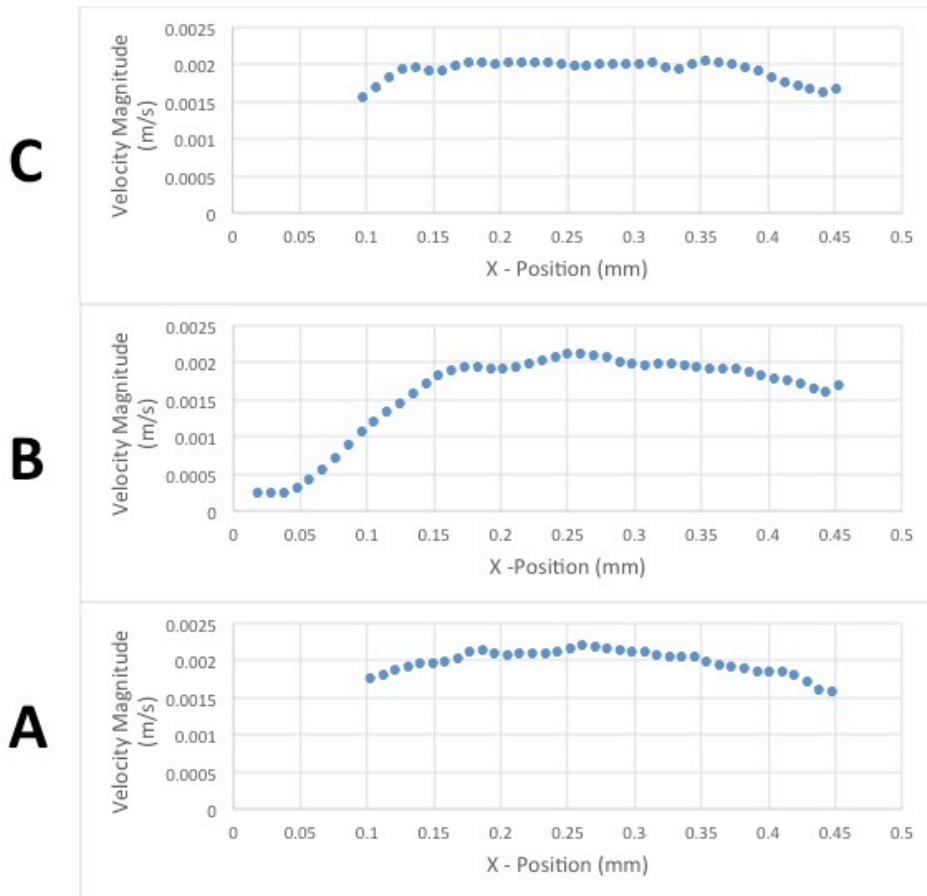


**Figure 4-2:** Velocity magnitude vs. X – Position in the crevice channel.

Data obtained within the backward facing step model is displayed in Figure 4-3. The velocity magnitude was taken at 50 points per line at three locations according to the same method as described previously. Figure 4-4 displays velocity profiles obtained within the backward facing step model. Within the backward facing step, the velocity profile taken at  $Y = -0.3$  mm (location A) shows that the entering fluid had a mean velocity of 1.84 mm/s. After the step, the magnitude of velocity decreases as would be expected due to the increase in cross-sectional area of the channel. The region of slowest flow is located in the corner of the channel immediately downstream of the backward facing step (0.04 mm, -0.25 mm). At  $Y = -0.15$  mm (location B), located 0.1 mm downstream of the step, the velocity profile shows that the mean

velocity is 0.818 mm/s. Another 0.1 mm downstream at  $Y = -0.05$  (location C) the flow profile shows that the mean velocity was increased to 1.93 mm/s.

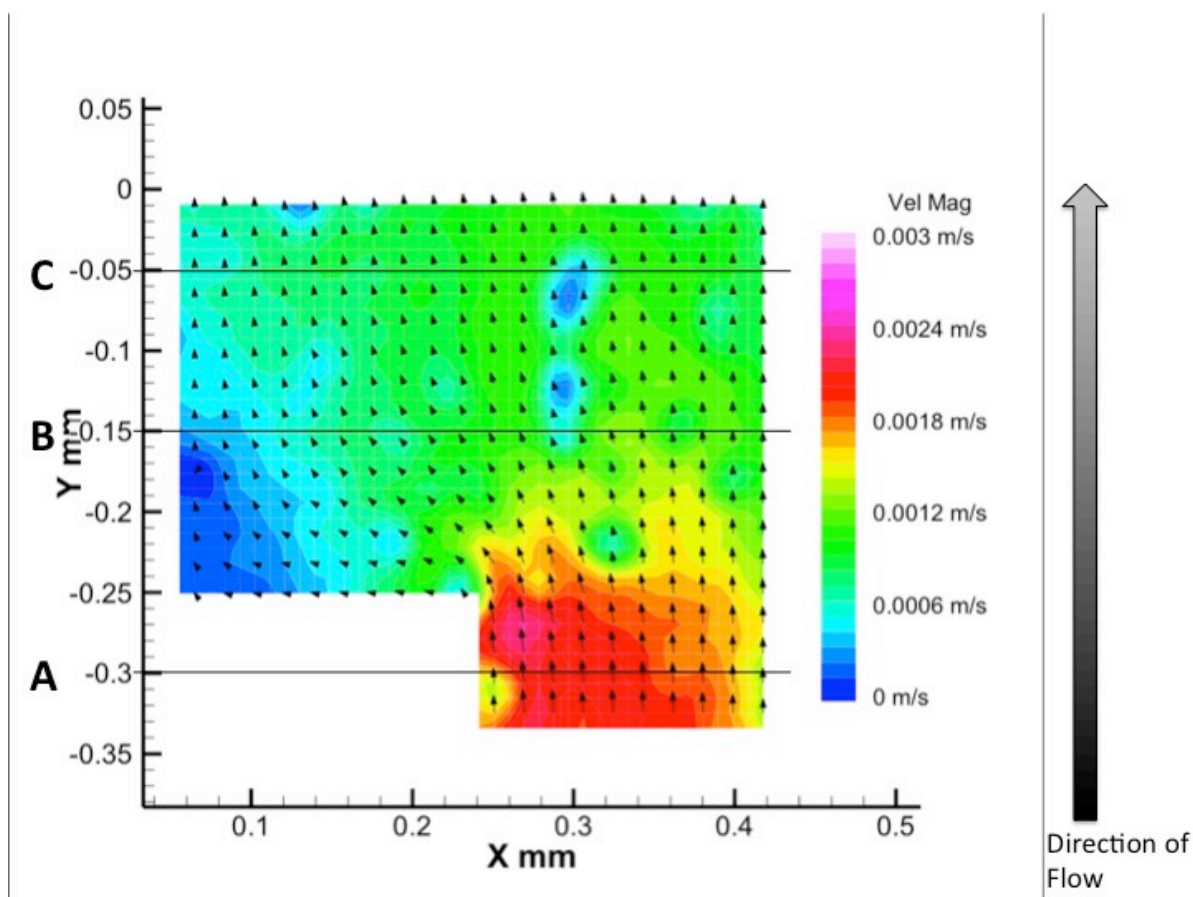


**Figure 4-3:** Flow within the backward facing step channel at  $1 \mu\text{L}/\text{min}$ . Velocity profiles were obtained from the positions labeled A, B, and C.

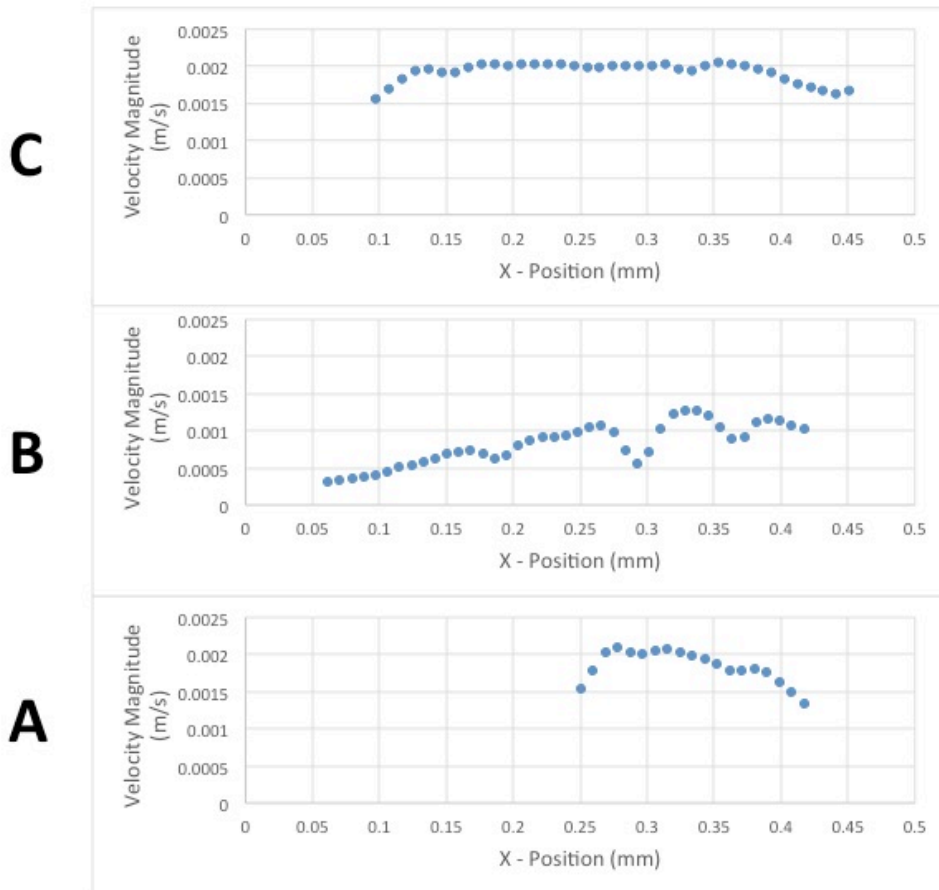


**Figure 4-4:** Velocity magnitude vs. X – Position in the backward facing step channel.

## 4.2 Blood Analog Experiment

Data were acquired using either platelet-rich plasma or 20% ghost cell hematocrit bovine blood as the test fluid. The generated vector fields were post-processed in Tecplot and analyzed according to the same method used in Section 4.1. Figure 4-5 shows the vector field obtained from a crevice channel in which platelet-rich plasma was used as the test fluid. The magnitude of velocity was observed to be the highest in center of the channel. As the distance from the center increased, the magnitude of velocity decreased. There is a region of slow flow inside the crevice. At the upstream corner of the crevice near the main channel the magnitude of velocity appears

qualitatively higher than the magnitude of velocity at the downstream corner of the crevice near the main channel. Figure 4-6 displays the vector field obtained in a crevice channel in which 20% hematocrit bovine blood was used as the test fluid. The magnitude of velocity was observed to be greater towards the center of the channel. The region close to the crevice and within the crevice had a lower velocity magnitude.

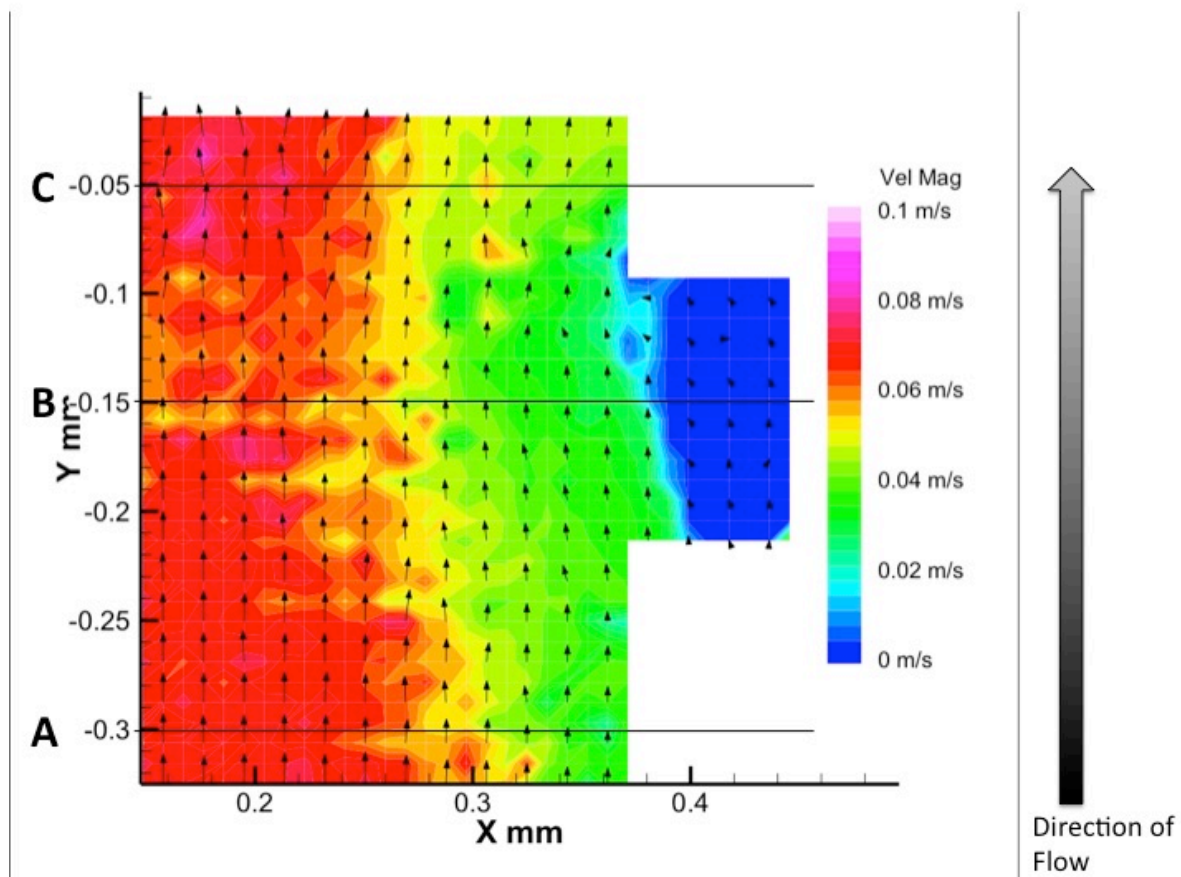


**Figure 4-5:** Flow within the crevice channel at 20  $\mu\text{L}/\text{min}$ . The fluid used was platelet-rich plasma. Velocity profiles were obtained from the positions labeled A, B, and C.



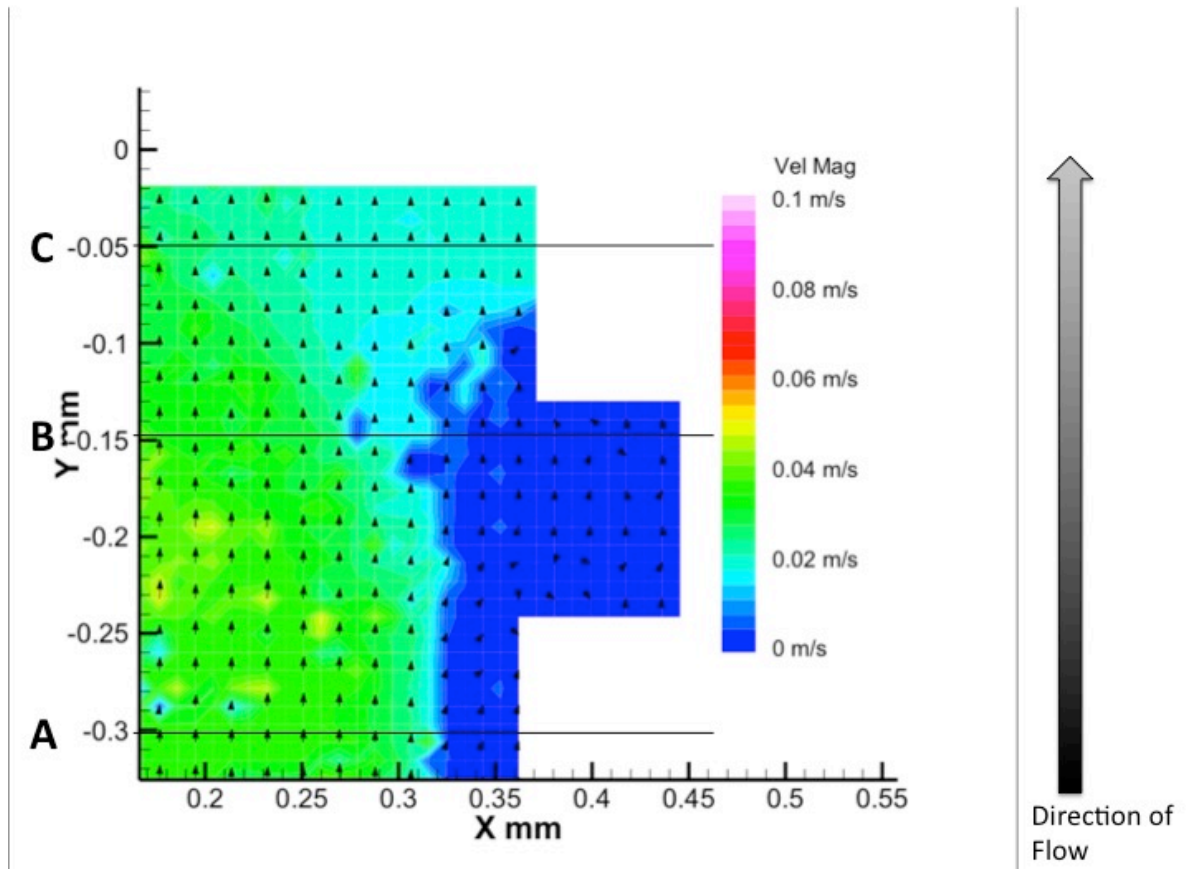


**Figure 4-6:** Flow within the crevice channel at 20  $\mu\text{L}/\text{min}$ . The fluid used was 20% ghost cell hematocrit bovine blood. Velocity profiles were obtained from the position labeled A, B, and C.

Figure 4-7 displays the velocity profiles acquired at locations A, B and C. The flow profile taken at  $Y = -0.3$  mm (location A) shows that the entering fluid had mean velocity of 54.9 mm/s for PRP and 25.6 mm/s for 20% Hct bovine blood. Within the crevice, at  $Y = -0.15$  mm (location B), the mean velocity slows down to 37.4 mm/s for PRP and 15.2 mm/s for 20% Hct bovine blood. At  $X = 0.37$ , which is X coordinate of the entrance to the crevice, the flow profile at location B displays that the magnitude of velocity is 27.7 mm/s for PRP and 1.36 mm/s for 20% Hct bovine blood. The region of slowest flow is located along the back wall of the crevice furthest from the main channel at  $X = 0.43$  mm. Near the back wall of the crevice at location B

the magnitude of velocity was recorded to be 1.52 mm/s for PRP and 0.385 mm/s for 20% Hct bovine blood. At  $Y = -0.05$  (location C) the flow profile shows that the mean velocity is increased back to 56.3 mm/s for PRP and 20.5 mm/s for bovine blood.

In order to determine the quality of the data produced using PRP and 20% Hct bovine blood as the fluid, a comparison of the percentage of vectors determined to be valid by INSIGHT software was made. Figure 4-8 displays the percentage of valid vectors by fluid type perfused. PRP was shown to produce a higher percentage of valid vectors compared to 20% Hct bovine blood. The percentage of valid vectors for PRP was 97% and the percentage of valid vectors for 20% Hct bovine blood was 95%.

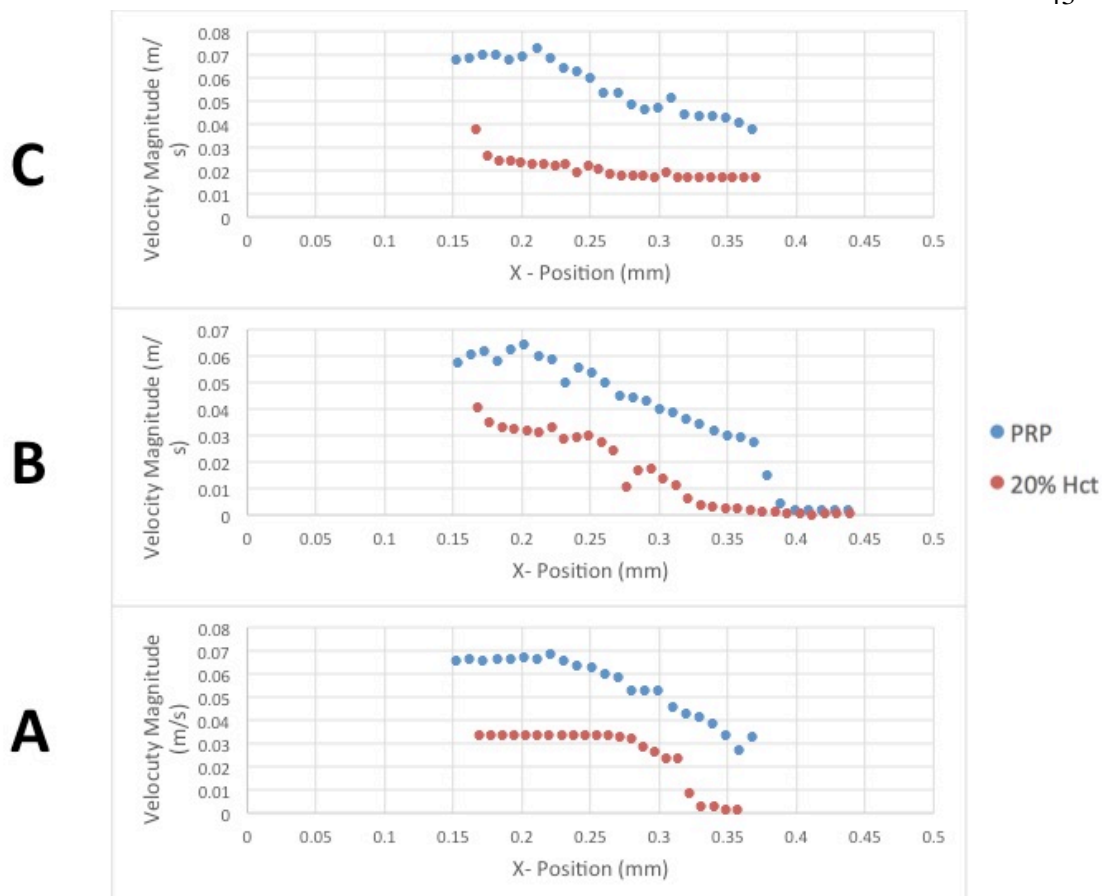


**Figure 4-7:** Velocity magnitude vs. X – Position in the crevice channel at 20  $\mu\text{L}/\text{min}$  flow rate. The velocity profiles of PRP and 20% Hct bovine blood were compared.

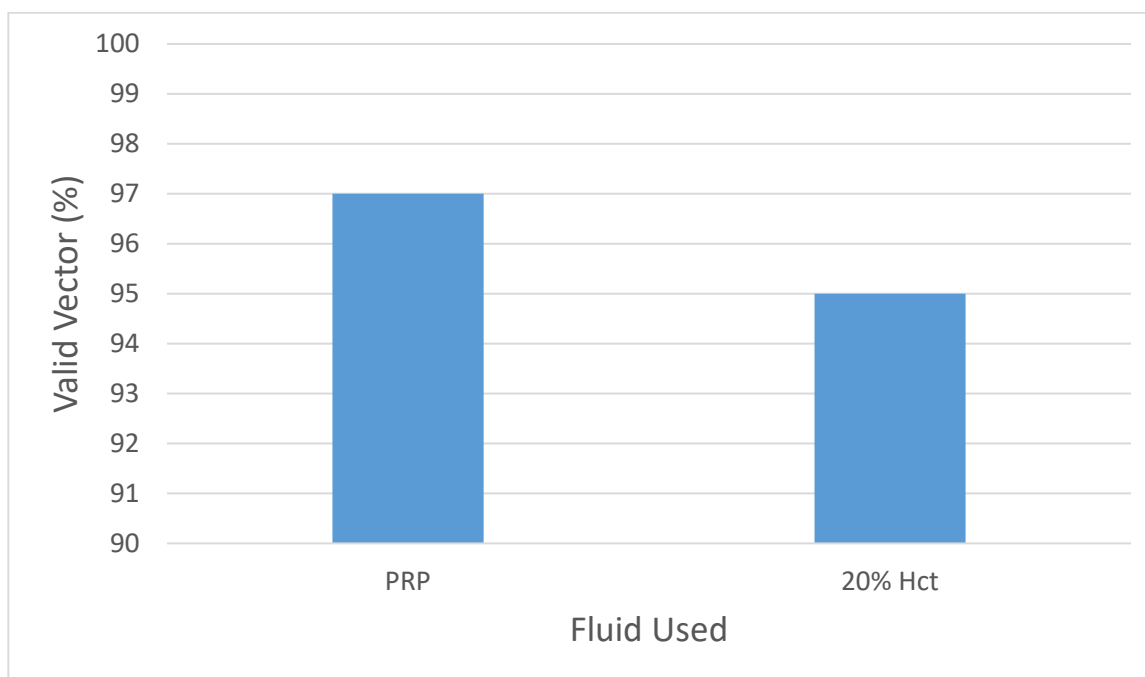


**Figure 4-8:** A comparison of the percentage of valid vectors by fluid used. For each measurement, 200 image pairs were averaged without the use of a smoothing function.

## **Chapter 5**

### **Discussion**

#### **5.1 Validation of Technique**

Analysis of the experimental phase showed that laminar flow could be created within a PDMS device. Flow within the PDMS device could be quantitatively measured by  $\mu$ PIV. Two-dimensional vector fields generated had a very high percentage of valid vectors. In the crevice model 98% of the vectors were labeled valid. In the backward facing step, 99% were labeled valid. A high valid vector percentage indicates that the software was able to correlate particles from frame A and B image pairs with a high degree of certainty.

Geometric irregularities affect the velocity profile within a PDMS channel. Crevice and backward facing step channels were both shown to produce regions of reduced flow velocity. Figure 4-2 shows that the crevice produced a region of slow flow within the channel. The mean velocity reduction from 1.99 mm/s at location A to 1.60 mm/s at location B is due to an increase in the cross-sectional area of the channel at location B. The crevice is positioned adjacent to the flow; therefore there is no direct flow into the crevice and relatively small momentum transfer. Computational fluid simulations have shown that in a lid driven cavity there is a volume of fluid that remains in the interior of the cavity<sup>42</sup>. The computational result is shown in Figure 5-1. The small volume of fluid in the crevice is able to dissipate the relatively small momentum transfer into the crevice. Data from this study support the computational prediction. Shown in Figure 4-1,

there was a region along the back wall of the crevice wherein the fluid had a magnitude of velocity equal to 0.25 mm/s, which is near zero.

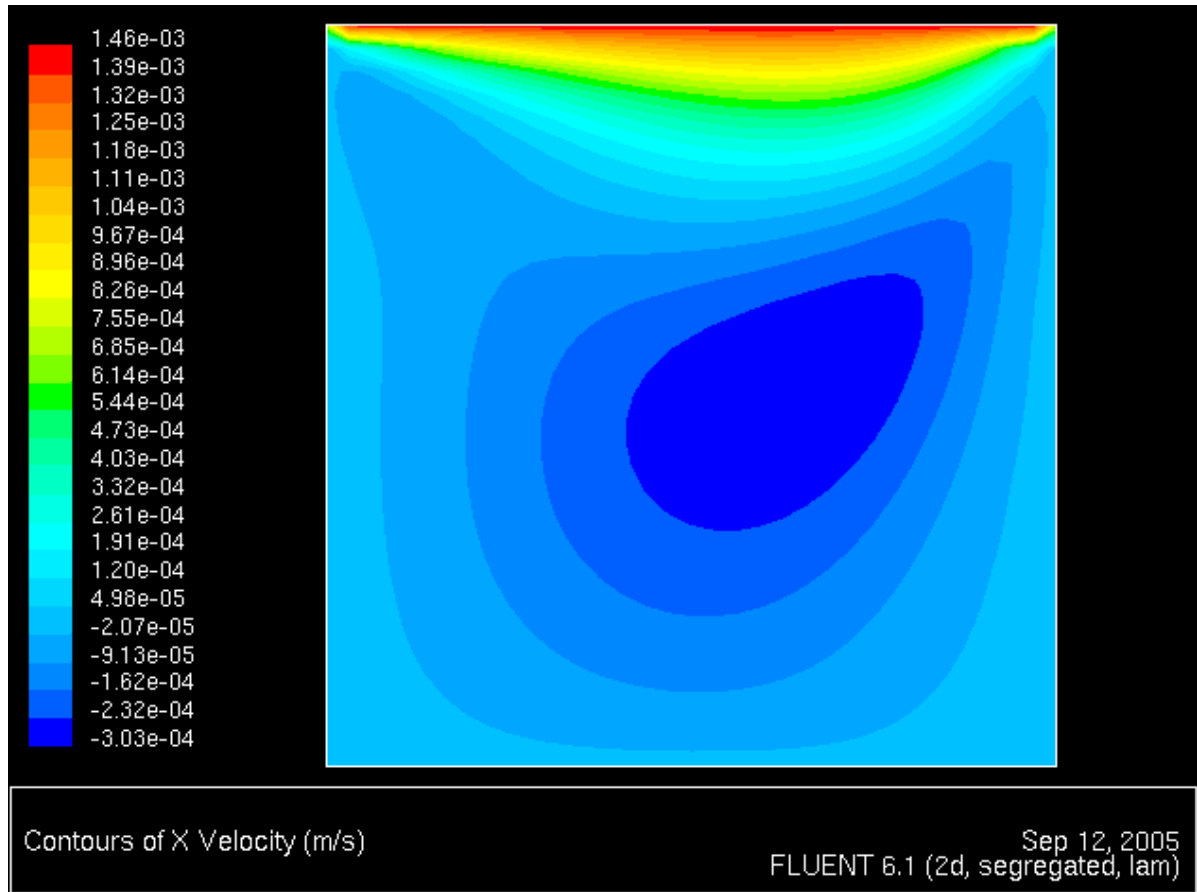


**Figure 5-1:** Computational simulation of fluid flowing adjacent to a crevice at  $Re = 100$ . A region of stagnant to near stagnant flow can be observed within the crevice<sup>42</sup>.

In the backward facing step channel, the sudden expansion in cross-sectional area decreased the mean flow velocity from 1.85 mm/s at location A to 0.818 mm/s at location B. A computational simulation predicted a region of slow flow immediately downstream of the backward facing step<sup>43</sup>. Figure 5-2 displays a computational simulation of a backward facing step model at  $Re = 252$ . Data from this study (Figure 4-3) appears qualitatively different from the

simulation. An explanation for the disagreement is that the Reynolds number used in this study was equal to 0.19.

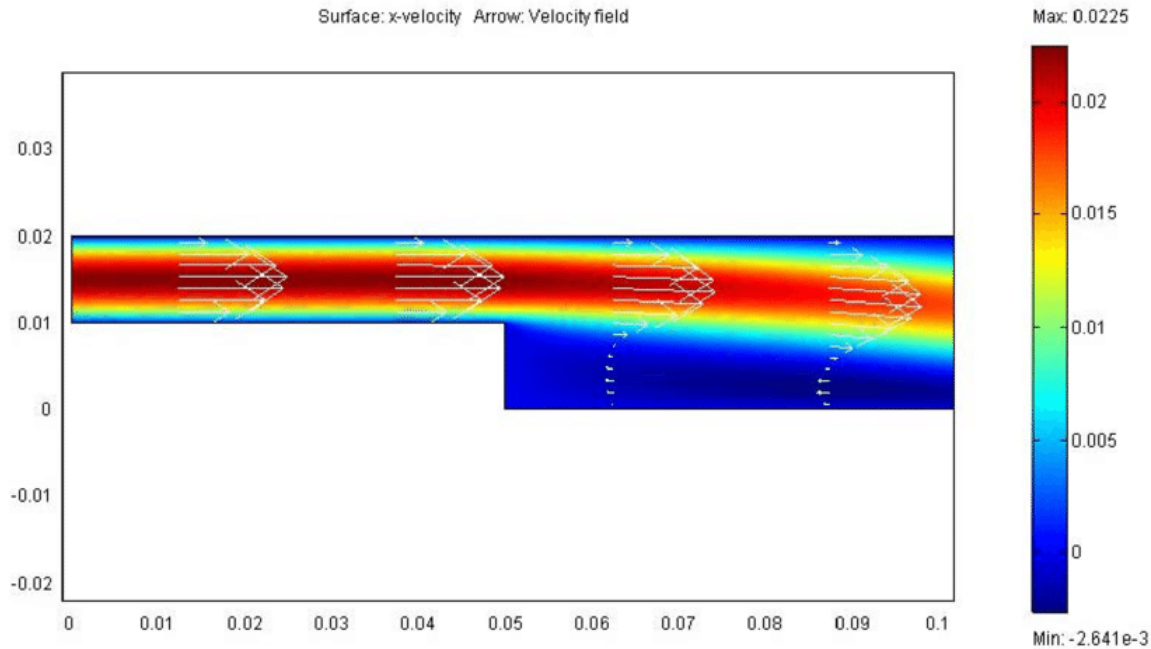


**Figure 5-2:** Computational simulation of a velocity profile in a backward facing step model.  $Re = 242$ . There is a region of slow flow after the expansion<sup>43</sup>.

## 5.2 Blood Analog

Results obtained show that  $\mu$ PIV measurements can be made even if a more viscous and less transparent fluid is perfused through a PDMS channel. Data acquired displays that the velocity profile from 20% Hct bovine blood in the crevice channel has a more blunt shape with a relatively higher velocity component near the chamber wall compared to the velocity profile of platelet-rich plasma. The finding that an increase in fluid viscosity makes the velocity profile more blunt is supported by previous research<sup>44</sup>. Ghost cell aggregation in the center of the channel could account for the blunt velocity profile observed in Figure 4-7 at locations A and C.

Platelets and platelet-sized particles have been observed to be found in higher concentrations near the wall of a vessel compared to the center<sup>46</sup>. Since Brownian diffusion alone cannot account for the increased concentration, shear rate and hematocrit have been identified as factors that could induce platelet margination. An elevated concentration of platelets near vessel walls does not occur in platelet-rich plasma indicating that red blood cells must play a role. The margination of platelets and tracer particles to the near wall regions of the PDMS channel in the z-axis could explain the slower velocity profile observed in 20% ghost cell Hct bovine blood compared to PRP.

Data obtained within the crevice model show that there are regions where a clot is more likely to form. Within the crevice, the area furthest from the main channel has the slowest velocity. This was the case for both PRP and 20% ghost cell Hct blood at 20  $\mu\text{L}/\text{min}$  flow. Areas of slow flow have increased platelet residency time and could promote the development of a thrombus if activated platelets adhere in a slow moving region<sup>17</sup>. In Figure 4-5 it can be observed that there is a region of stagnation within the crevice. The decrease in fluid speed is not sudden but instead gradually declines as the distance from the main channel increases as shown in Figure 4-6. Previous literature has indicated that the distal corner near the main channel is the most probable location of shear-activated platelets<sup>16, 17</sup>. The increase in velocity as PRP exits the crevice supports this finding because increased velocity leads to increased shear rate

Using a  $\mu\text{PIV}$  system, flow within a PDMS chamber can be quantitatively measured. When using a viscous and opaque blood analog,  $\mu\text{PIV}$  measurements can be made however the precision of measurement is affected. Furthermore, the changes in flow velocity caused by abrupt changes in channel geometry can be studied. Data from the present study validate the technique's ability to generate stable flow within a PDMS channel. The experiment with bovine



blood lends support to its potential as a platform to study the formation of blood clots. Results from this study lend support to the hypothesis that small changes in flow geometry caused by surface irregularities on artificial cardiovascular devices can create flow regimes that are conducive to rheological platelet activation.

### **5.3 Limitations and Future Research**

INSIGHT software is very precise in its generation of vectors. When identical raw data from an experiment is processed using two identical processing procedures, the resulting vector fields were identical. However, a high degree of precision does not necessarily imply accuracy. In the crevice and backward facing step, the mean velocity magnitude within the channel at location A is recorded to be 1.99 mm/s and 1.85 mm/s respectively. The expected mean velocity based on  $Q = VA$  shows that the mean velocity should be 4.16 mm/s in the crevice and 8.33 mm/s in the backward facing step before the expansion. These findings notwithstanding, it is not likely that the accuracy of the system was compromised. The high percentage of valid vectors indicates that this system was working well and supports the hypothesis that the mean velocity in the channel was indeed the experimental value and not what an equation would predict. This discrepancy between observed and predicted mean velocity could be due to platelet and tracer particle margination to the near wall regions of the PDMS channel.

One possible source of error was the region of burnt pixels on the CCD camera. Burnt pixels were located in the lower left corner and middle right segments of the field of view as shown in Figure 5-3. Data will be skewed in and around the regions of burnt pixels. A tracer particle that travels into a region of burnt pixels will not be able to be correlated between a frame

A and B pair. To compensate for the burnt pixels, a smoothing function was applied to the vector field after processing as mentioned previously.

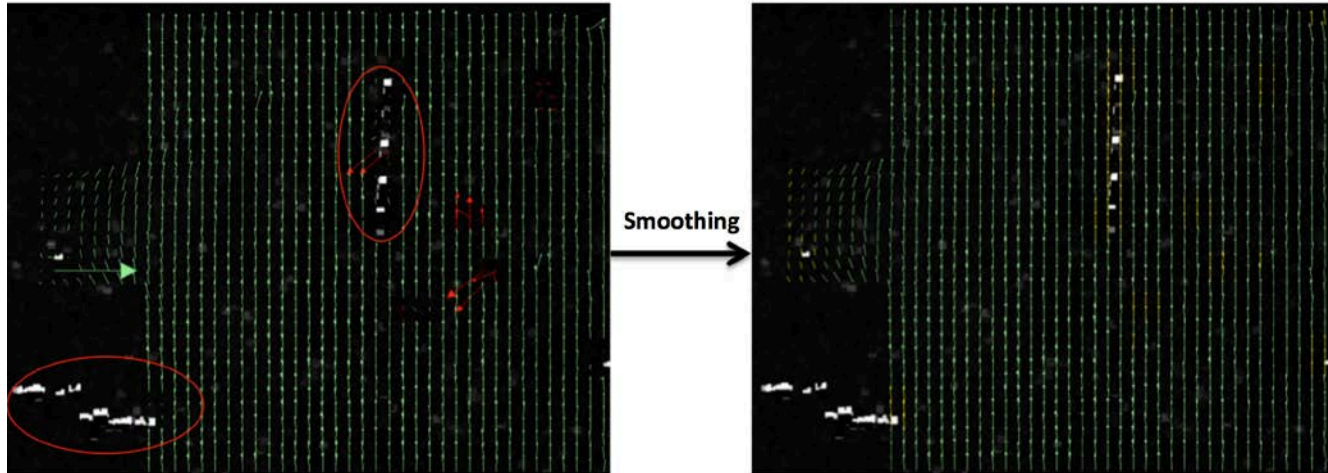


**Figure 5-3:** Regions of burnt pixels skewed data collection. A smoothing function was able to mask these regions, however the actual flow vectors in the regions highlighted in red on the left were not calculated.

Challenges in PDMS channel manufacturing such as the accumulation of dust particles and inability of the PDMS to form an airtight seal with the glass slide caused a low number of channels to be viable for testing. A low success rate in channel manufacturing and stable fluid injection lead to no data being recorded in the backward facing step model with platelet-rich plasma or 20% Hct bovine blood. In the future, more experiments could be completed using platelet-rich plasma and 20% ghost cell erythrocyte bovine blood in the backward facing step model. Future studies could also focus on quantifying thrombus development within a PDMS channel by tagging fibrin and platelets with fluorescent markers and looking at their deposition over time.

## BIBLIOGRAPHY

1. Kochanek, K. D., et al., (2011). *National Vital Statistics System*, **60**(3), p1-116.
2. Taylor DO, Edwards LB, Boucek MM, et al. Registry of the International Society for Heart and Lung Transplantation: twenty-fourth official adult heart transplant report--2007. *J. Heart Lung Transplant*. 2007; 26(8): 769-81. doi: 10.1016/j.healun.2007.06.004.
3. Mielniczuk L, Mussivand T, Davies R, et al. Patient selection for left ventricular assist devices. *Artif. Organs* 2004;28(2):152-7. Available at: <http://www.ncbi.nlm.nih.gov/pubmed/14961953>.
4. Rogers, J. G. (2016). Managing VAD complications: our growth industry.
5. CardioSmart. (2015, June). Understanding Heart Valve Disease. Retrieved January 1, 2019, from <https://www.cardiosmart.org/heartvalvedisease>
6. Maleki, M., Alizadehasl, A., & Haghjoo, M. (2017). *Practical Cardiology*. Elsevier Health Sciences.
7. Iakovou, I., Schmidt, T., Bonizzoni, E., Ge, L., Sangiorgi, G. M., Stankovic, G., ... & Michev, I. (2005). Incidence, predictors, and outcome of thrombosis after successful implantation of drug-eluting stents. *Jama*, 293(17), 2126-2130.
8. Starling RC, Moazami N, Silvestry SC, et al. Unexpected abrupt increase in left ventricular assist device thrombosis. *N Engl J Med* 2014;370: 33–40.

9. Sousa Sobrinho, J. R., Legaspe, E., Drigo, E., Dias, J. C., Dias, J. C., Barboza, M., ... & Santos Filho, D. J. (2018). Supervisory Control System Associated with the Development of Device Thrombosis in VAD. In *Technological Innovation for Resilient Systems: 9th IFIP WG 5.5/SOCOLNET Advanced Doctoral Conference on Computing, Electrical and Industrial Systems, DoCEIS 2018, Costa de Caparica, Portugal, May 2-4, 2018, Proceedings 9* (pp. 90-97). Springer International Publishing.
10. Buckley, M. F., James, J. W., Brown, D. E., Whyte, G. S., Dean, M. G., Chesterman, C. N., & Donald, J. A. (2000). A novel approach to the assessment of variations in the human platelet count. *Thrombosis and haemostasis*, 83(03), 480-484.
11. Furie, B., & Furie, B. C. (2007). *Journal of Thrombosis and Haemostasis*, 5(s1), 1217.
12. Furie, B., & Furie, B. C. (2008). *New England Journal of Medicine*, 359(9), 938- 949.
13. Raber M.N., “Coagulation Tests,” Clinical Methods: The History, Physical, and Laboratory Examinations, 3rd edition, Walker H.K., Hall W.D., Hurst J.W., Editors. 1990, Butterworths: Boston, pp. 739–742 <sup>[1]</sup><sub>SEP</sub>
14. Dodge, J. T., Brown, B. G., Bolson, E. L., & Dodge, H. T. (1992). Lumen diameter of normal human coronary arteries. Influence of age, sex, anatomic variation, and left ventricular hypertrophy or dilation. *Circulation*, 86(1), 232-246.
15. Barrios-Pina H, Viazzo S, Rey C. A numerical study of laminar and transitional mixed <sup>[1]</sup><sub>SEP</sub> convection flow over a backward-facing step. *Comput. Fluids* 2012;56:77-91. doi:10.1016/j.compfluid.2011.11.016. <sup>[1]</sup><sub>SEP</sub>

16. Wu, W. T., Jamiolkowski, M. A., Wagner, W. R., Aubry, N., Massoudi, M., & Antaki, J. F. (2017). Multi-constituent simulation of thrombus deposition. *Scientific Reports*, 7, 42720.
17. Jamiolkowski, M. A., et al., (2016). *Biomaterials*, **96**, p72-83.
18. Sugii, Y., et al. (2005). *Measurement science and Technology*, 16(5), 1126.
19. Hochareon P., Manning K., Fontaine A., Tarbell J., Deutsch S., 2004, “Wall shear-rate estimation within the 50cc Penn State artificial heart using particle image velocimetry,” *J. Biomech. Eng.*, 126, 430–437.
20. Abularrage, C. J., et al. (2005). *Journal of vascular surgery*, **42**(3), p574-581.
21. Leyton-Mange, J.S., (2005) Design of Side-View Particle Image Velocimetry System For Cellular Adhesion Analysis (Honors Undergraduate Thesis). Print.
22. Benjamin, E. J., et al., (2018). *Circulation*, **137**(12), e67-e492.
23. DNA Purification Using Buffy Coat. <http://acceleratingscience.com/biobanking/dna-purification-using-buffy-coat/>. Accessed December 29, 2018.
24. Hangenah, Kristen., (2017) Characterization of Thrombi Through MRI and Histological Analysis of Erythrocyte Ghost Clots (Honors Undergraduate Thesis. Electronic.
25. Mayo Clinic. (n.d.). Cardiovascular Diseases. Retrieved January 1, 2019, from <https://www.mayoclinic.org/medical-professionals/cardiovascular-diseases/news/prosthetic-valve-thrombosis-time-is-critical/mac-20430866>

26. Koliopoulou, Antigone et al. "Bleeding and thrombosis in chronic ventricular assist device therapy: focus on platelets" *Current opinion in cardiology* vol. 31,3 (2016): 299-307.
27. Bluestein, D. (2004). Research approaches for studying flow-induced thromboembolic complications in blood recirculating devices. *Expert review of medical devices*, 1(1), 65-80.
28. De Biasi, A. R., Manning, K. B., & Salemi, A. (2015). Science for surgeons: understanding pump thrombogenesis in continuous-flow left ventricular assist devices. *The Journal of thoracic and cardiovascular surgery*, 149(3), 667-673.
29. Morel, O., Morel, N., Jesel, L., Freyssinet, J. M., & Toti, F. (2011, September). Microparticles: a critical component in the nexus between inflammation, immunity, and thrombosis. In *Seminars in immunopathology* (Vol. 33, No. 5, p. 469). Springer-Verlag.
30. Ye, X., Shao, Y. L., Zhou, M., Li, J., & Cai, L. (2009). Research on micro-structure and hemo-compatibility of the artificial heart valve surface. *Applied Surface Science*, 255(13-14), 6686-6690.
31. Bergmeier, W. Resting Platelet [Digital image]. Retrieved February 12, 2019, from <http://bergmeierlab.web.unc.edu/files/2016/01/resting-platelet-sem.jpg>
32. Bergmeier, W. Activated Platelet [Digital image]. Retrieved February 12, 2019, from <http://bergmeierlab.web.unc.edu/files/2016/01/activated-platelet-sem.jpg>
33. Milner, K. R., Snyder, A. J., & Siedlecki, C. A. (2006). Sub-micron texturing for reducing platelet adhesion to polyurethane biomaterials. *Journal of Biomedical Materials Research Part A: An Official Journal of The Society for Biomaterials, The Japanese*

*Society for Biomaterials, and The Australian Society for Biomaterials and the Korean Society for Biomaterials*, 76(3), 561-570.

34. Bansal, A., & Shrivastava, A. K. Implementation of NTSS Algorithm to three dimensional Particle Image Velocimetry for fluid flow using GPU.
35. Morales, D. L. S. *et al.* Bridging children of all sizes to cardiac transplantation: the initial multicenter North American experience with the Berlin Heart EXCOR ventricular assist device. *J. Heart Lung Transplant.* **30**, 1–8 (2011).
36. Schoeman, R. M., Rana, K., Danes, N., Lehmann, M., Di Paola, J. A., Fogelson, A. L., ... & Neeves, K. B. (2017). A microfluidic model of hemostasis sensitive to platelet function and coagulation. *Cellular and molecular bioengineering*, 10(1), 3-15.
37. Korson, L., Drost-Hansen, W., & Millero, F. J. (1969). Viscosity of water at various temperatures. *The Journal of Physical Chemistry*, 73(1), 34-39.
38. Rand, P. W., Lacombe, E., Hunt, H. E., & Austin, W. H. (1964). Viscosity of normal human blood under normothermic and hypothermic conditions. *Journal of Applied Physiology*, 19(1), 117-122.
39. (n.d.). Retrieved March 24, 2019, from [http://2016.igem.org/File:SUSTech\\_Shenzhen-2016-10-14\\_17.31.51.jpg](http://2016.igem.org/File:SUSTech_Shenzhen-2016-10-14_17.31.51.jpg)
40. Plasma treatment of PDMS for microfluidic applications. (n.d.). Retrieved March 24, 2019, from <https://plasmamatreatment.co.uk/henniker-plasma-technology/plasma-treatments/plasma-surface-activation-to-improve-adhesion/plasma-treatment-of-pdms/>
41. Caro, C. G. (1973). Transport of material between blood and wall in arteries. *Atherogenesis: initiating factors*, 127-149.

42. CFD Online. (n.d.). Lid-driven cavity problem. Retrieved April 4, 2018, from [https://www.cfd-online.com/Wiki/Lid-driven\\_cavity\\_problem](https://www.cfd-online.com/Wiki/Lid-driven_cavity_problem)
43. Gualtieri, Carlo. (2005). Numerical Simulations of Laminar Backward-Facing Step Flow With FEMLAB 3.1. Proceedings of the American Society of Mechanical Engineers Fluids Engineering Division Summer Conference. 2. 10.1115/FEDSM2005-77314.
44. Yeom, E., Kang, Y. J., & Lee, S. J. (2014). Changes in velocity profile according to blood viscosity in a microchannel. *Biomicrofluidics*, 8(3), 034110.
45. Taylor, J. O., Meyer, R. S., Deutsch, S., & Manning, K. B. (2016). Development of a computational model for macroscopic predictions of device-induced thrombosis. *Biomechanics and modeling in mechanobiology*, 15(6), 1713-1731.
46. Tilles, A. W., & Eckstein, E. C. (1987). The near-wall excess of platelet-sized particles in blood flow: its dependence on hematocrit and wall shear rate. *Microvascular research*, 33(2), 211-223.



## ACADEMIC VITA

## Tice Harkins

harkinstice@gmail.com

## Education

05/2019      B.S. in Pre-Medicine, Minor in Biomedical Engineering  
Honors in Biomedical Engineering, Schreyer Honors College  
The Pennsylvania State University

# Thesis

04/2019      Development of a Micro-Particle Image Velocimetry System to Study  
Thrombosis In-Vitro  
Thesis Supervisor: Keefe B. Manning, Ph.D.

## Teaching

2017-2018 Laboratory Teaching Assistant, BIOL 230W Molecules and Cells  
The Pennsylvania State University

Fall 2018    Laboratory Teaching Assistant, BIOL 220W Ecology  
The Pennsylvania State University

## Grants

**Current:**

Penn State Erickson Discovery Grant (PI) 5/18-8/18  
Characterizing Flow and Clotting in PDMS Channels Using  
Micro-Particle Image Velocimetry

## **Completed:**

Penn State Erickson Discovery Grant (PI) 5/17-8/17  
Investigating Thrombosis *In Vitro* Using Micro-Particle Image  
Velocimetry

## **Honors and Awards**

- 2018 First Place in the Research Poster Competition  
(Joint Conference of Three Societies, Krakow, Poland)
- 2018 Finalist in the ASME Student Paper Competition (8<sup>th</sup> WCB, Dublin, Ireland)
- 2018 Paul D. and the Rev. David P. Wentroble Scholarship (Penn State)
- 2017 PNC Leadership Development Program (Penn State)
- 2017 Vice President, The National Society of Collegiate Scholars (Penn State)
- 2015 First Award in the Scientific Presentation Competition  
(PJAS, Pittsburgh, PA)

## **Presentations**

Characterizing Flow and Clotting in PDMS Channels Using Micro-Particle Image  
Velocimetry. *2019 Undergraduate Research Exhibition*  
University Park, PA.

Investigating Thrombosis *In Vitro* Using Micro-Particle Image Velocimetry  
*2018 Undergraduate Research Exhibition*  
University Park, PA

Effects of Salinity on Primary Root Growth in *Arabidopsis thaliana*  
*2016 Freshman Research Initiative*  
University Park, PA

## Conference Abstracts

Harkins, T.R., Myslowski, J.E., Good, B.C., Manning, K.B. 2018. Development of a Micro-Particle Image Velocimetry Platform to Study Thrombosis *In Vitro*. *8<sup>th</sup> World Congress of Biomechanics*, Dublin, Ireland, July 8-12, 2018.

Harkins, T.R., Myslowski, J.E., Manning, K.B. 2018. Analysis of Flow and Thrombus Development Within PDMS Channels of Varying Geometry. *Joint Meeting of The European Society for Clinical Hemorheology and Microcirculation, The International Society of Clinical Hemorheology, and The International Society of Biorheology*. Krakow, Poland, July 2-6, 2018.

Harkins, T.R., Myslowski, J.E., Manning, K.B. 2018. Quantification of Flow and Thrombus Development using Micro-Particle Image Velocimetry. *American Society for Artificial Internal Organs 64<sup>th</sup> Annual Conference*. Washington, D.C., June 13-16, 2018.